
Weakening of the Indian Ocean Dipole in the mid-Holocene due to the mean oceanic climatology change

Shanshan Liu[a], Chaoxia Yuan[a], Jing-jia Luo[a], Xiaofan Ma[a], Xuecheng Zhou[b], Toshio Yamagata[a, c]

[a] *Collaborative Innovation Center on Forecast and Evaluation of Meteorological Disasters (CIC-FEMD)/Institute for Climate and Application Research (ICAR), Nanjing University of Information Science and Technology, Nanjing, China*

[b] *Meteorological Service Center of Jiangsu Province, Nanjing, China*

[c] *Application Laboratory, Research Institute for Value-Added-Information Generation, Japan Agency for Marine–Earth Science and Technology, Yokohama, Japan*

Corresponding author: Shanshan Liu (E-mail: liushanshan@nuist.edu.cn)

ABSTRACT

The Indian Ocean Dipole (IOD) is one of the leading modes of interannual climate variability in the tropical Indian Ocean (IO). Paleoclimate provides real climate scenarios to examine IOD behaviors and the linkage to basic states. Based on 18 models from the Paleoclimate Modelling Intercomparison Project phase 3 and 4 (PMIP 3/4), the IOD change from the preindustrial period to mid-Holocene is investigated. The multimodel mean reveals that the IOD variability weakens by 14% as measured by the standard deviation of the Dipole Mode Index, which is defined using the zonal sea surface temperature (SST) difference. Such attenuation is dominated by the spatially consistent suppression in the western-pole SST variability, while the eastern pole contributes little due to the opposite-signed changes in its northwestern and southeastern portions. The primary reason for the aforementioned changes comes from the altered climatic background, which displays a positive IOD-like pattern during IOD growing seasons, with intensified westward currents along the equator and northwestward currents in the southeastern equatorial IO. Such changes in the mean-state currents modulate the strength of the IOD-related anomalous advection and subsequently cause alterations in the IOD variability. Further analyses show that the IOD attenuation in the mid-Holocene is likely irrelevant to the concurrently subdued El Niño–Southern Oscillation in the tropical Pacific because of the diminished connections between the two oscillations themselves. The above simulated changes in both the IO mean climatology and IOD variability agree well with the available paleo-records in literature.

SIGNIFICANCE STATEMENT

Understanding variations in the IOD and its relationship to the altered background mean state can advance our knowledge of tropical climate dynamics. Paleoclimate provides the opportunity to address this issue under real climate scenarios in the past. Based on multiple models from the PMIP 3/4, we investigate IOD changes during the mid-Holocene compared to the preindustrial period. The result shows a weakening of the IOD, and the main mechanism lies in the altered anomalous advection modulated by changes in the mean-state currents. The simulated changes in both the mean state and IOD variability are consistent with available paleo-data. The present study extends the research scale of IOD dynamics beyond instrumental periods and provides scientific bases for deciphering geological records.

1. Introduction

The Indian Ocean Dipole (IOD) is a basin-scale ocean–atmosphere coupled mode that occurs at the interannual timescale over the tropical Indian Ocean (IO) (Saji et al. 1999; Webster et al. 1999). It is characterized by a zonal dipole pattern of sea surface temperature (SST) and precipitation anomalies. The positive IOD phase features anomalously cool and dry conditions in the southeastern equatorial IO (SEIO) and anomalously warm and wet conditions in the western equatorial IO (WEIO), and the negative phase is an approximate mirror image. IOD exerts climatic impacts that are felt throughout the world, which are particularly pronounced in the IO-rim regions (Yamagata et al. 2004; Schott et al. 2009; Saji 2018). Positive events are related to droughts and wildfires in Indonesia and Australia (Abram et al. 2003; Ummenhofer et al. 2009; King et al. 2020), as well as flooding and malaria outbreaks in eastern Africa (Marchant et al. 2007; Hashizume et al. 2012). Therefore, it is vital to thoroughly understand the inherent dynamical mechanisms of IOD variability.

A number of studies have explored the generating and sustaining mechanisms of IOD, including internal feedback processes and external triggering factors. It has been reported that IOD originates from ocean–atmosphere interactions, growing through the wind–thermocline–SST (Bjerknes 1969), wind–evaporation–SST (Xie and Philander 1994), and cloud–radiation–SST (Li et al. 2003; Fischer et al. 2005) feedbacks. Given that the former two feedbacks depend on the mean states, the IOD activity is seasonally locked (Saji et al. 1999; Li et al. 2003; Saji 2018). It tends to develop around May–June, peak during October–November, and rapidly decay thereafter. In addition, although the IOD is an internal mode in the tropical IO, it may be triggered by external forcings, such as the El Niño–Southern Oscillation (ENSO) (Luo et al. 2010; Zhang et al. 2015; Stuecker et al. 2017), intraseasonal oscillation (ISO) (Li et al. 2003; Rao et al. 2007; Lu et al. 2018), spring snow cover in the Eurasian continent (Yuan et al. 2019), and southern annular mode (Lau and Nath 2004). Among them, ENSO is likely to be the most influential factor, which can affect the IO climate through both oceanic and atmospheric pathways (An 2004; Fischer et al. 2005; Behera et al. 2006).

IOD is undergoing long-term changes over the past decades and is projected to change continually in the future. Available instrumental observations and coral proxies consistently have identified an increasing trend of intensity and frequency of positive IOD activities since the mid-20th century (Abram et al. 2008; Ihara et al. 2008; Nakamura et al. 2009; Abram et al. 2020b). Such intensification is possibly attributed to the observed easterly wind trend over the equatorial IO, which accelerates SEIO cooling during the IOD growing season by intensifying upwelling along the Java–Sumatra coast (Abram et al. 2008). However, a consensus is still lacking about the IOD behavior in the future with increasing global warming. Cai et al. (2014) indicated that extreme positive IOD events are expected to occur more frequently in the future, whereas the results are contested as being an artifact of model biases in the mean state (Li et al. 2016a). In addition, the IOD amplitude is projected to be larger than present due to the intensified local air–sea coupling induced by the strengthened easterly trade winds (Marathe et al. 2021; An et al. 2022). However, several other studies indicated that the IOD intensity might remain unchanged (Zheng et al. 2013; Chu et al. 2014), since the intensified thermocline feedback due to shoaling thermocline in the eastern equatorial IO (EEIO) is offset by the weakened atmospheric response to SST anomalies because of increased tropospheric stability (Zheng et al. 2013). The aforementioned disagreement over the projected IOD changes suggests that the relationship between the altered background mean state and IOD variability has not been fully understood.

Paleoclimate offers a valuable approach to examining the history of IOD and the linkage to background states under various climate scenarios that have occurred in the past (Abram et al. 2020a). The present study particularly focuses on the mid-Holocene (approximately 6 ka ago) when geological records are abundant and depict a markedly different climate from today (Brierley et al. 2020). Around the IO, multiple types of proxies have documented a positive IOD-like response of the mean climate (Abram et al. 2020a), including basin-wide SST cooling that was greater in the east than in the west (Abram et al. 2007; Cui et al. 2022; Weldeab et al. 2022), thermocline deepening in the WEIO (Kuhnert et al. 2014), as well as terrestrial wetting over eastern Africa (Gasse 2000; Thompson et al. 2002) and desiccating over southern and western Indonesia (Griffiths et al. 2010; Niedermeyer et al. 2014). Such changes make the mid-Holocene an analogue to the greenhouse scenario (Cai et al. 2013). In this context, the investigation regarding this interval might yield meaningful insights into future changes. Regarding the IOD variability, Abram et al. (2007) provided a coral-based reconstruction from the Mentawai Islands off the Sumatra coast that captures four positive IOD events at around 6.5–4.2 ka BP and four positive events during the past two millennia. Based on the composites of IOD events from each period, they showed that, compared to the late Holocene, IOD events during the mid-Holocene are characterized by a longer duration but similar magnitude of SST peak cooling. Note that the small sample size of this record might constrain the representativeness of the mid-Holocene IOD behaviors, and the proxy-based reconstruction seldom involves direct mechanisms. Numerical simulations offer a comparison to geological records and an opportunity to address underlying physical explanations. A simulation using the

Fast Ocean Atmosphere Model (FOAM) revealed a reduction of IOD strength at 6 ka BP (Brown et al. 2009). Conversely, based on an updated version of the Model for Interdisciplinary Research on Climate version 5 (MIROC5.2), Iwakiri and Watanabe (2019) suggested that the IOD is intensified, because enhanced horizontal advection term in the EEIO benefits the growth of the positive IOD. The aforementioned results that came from single-model simulations are mutually contradictory, making it valuable to conduct an analysis based on multiple models towards some consistent results. In the meantime, the mid-Holocene is a time when both records (Tudhope et al. 2001; Thompson et al. 2017) and model simulations (Tian et al. 2017; Chen et al. 2019) document suppressed ENSO variability. Whether the change in the IOD behavior is linked to such a reduction in ENSO intensity remains an open question.

As a target scenario of the Paleoclimate Modelling Intercomparison Project (PMIP), a large number of models have conducted the mid-Holocene equilibrium simulations under a common experimental protocol (Otto-Bliesner et al. 2017), enabling the analysis using multiple models. In the present analysis, the IOD variation during the mid-Holocene is examined using climate simulations undertaken by phases 3 and 4 of the PMIP (PMIP3/4) models, and the possible role of the altered mean states is elucidated through a diagnosis using mixed-layer heat budget (MLHB) equation analysis. In the meantime, the PMIP models are able to simulate the suppression of the ENSO activity, which allows a discussion on the relationship between the changes in ENSO and IOD. The paper is structured as follows. Section 2 describes the data and methods. In Section 3, we examine changes in the IO mean state based on multimodel ensemble means. Section 4 presents the alteration in the IOD activity and possible mechanisms. Summary and discussion are provided in Section 5.

2. Data and Methods

a. Data

The analysis is based on 18 climate models within the PMIP3/4 framework (Table 1), which conduct both mid-Holocene and preindustrial control experiments and include all the variables required here. The variables include monthly mean precipitation, 850-hPa geopotential height and horizontal wind speed, SST, surface wind stress and heat fluxes, as well as ocean potential temperature and velocity. For models from PMIP3, the ocean vertical velocity is not available and is thus yielded as the division of the upward ocean mass transport by the product of seawater reference density (1025 kg m^{-3}) and grid area. The last 100 years of mid-Holocene and preindustrial simulations are taken to represent the quasi-equilibrium climate states of both periods. The analysis focuses on the climatological differences between the two periods, and the statistical significance is assessed with the two-tailed Student's t test.

	Model ID	**Institution name**	**Horizontal resolution (longitude × latitude, level)**	
			Atmosphere	**Ocean**
1	BCC-CSM1-1	Beijing Climate Center, China	128 × 64, L26	360 × 232, L40
2	CSIRO-Mk3-6-0	Commonwealth Scientific and Industrial Research, Australia	192 × 96, L18	192 × 192, L31
3	FGOALS-g2	Institute of Atmospheric Physics, CAS, China	128 × 60, L26	360 × 180, L30
4	FGOALS-s2	Institute of Atmospheric Physics, CAS, China	128 × 108, L17	360 × 196, L30
5	GISS-E2-R	NASA Goddard Institute for Space Studies, USA	144 × 90, L40	288 × 180, L32
6	HadGEM2-CC	Met Office Hadley Center, UK	192 × 145, L60	360 × 216, L40
7	HadGEM2-ES	Met Office Hadley Center, UK	192 × 145, L38	360 × 216, L40
8	IPSL-CM5A-LR	Institut Pierre-Simon Laplace, France	96 × 95, L39	182 × 149, L31
9	MPI-ESM-P	Max Planck Institute for Meteorology, Hamburg, Germany	196 × 98, L47	256 × 220, L40
10	MRI-CGCM3	Meteorological Research Institute, Japan	320 × 160, L48	364 × 368, L51
11	CESM2	National Center for Atmospheric Research, USA	288 × 192, L32	320 × 384, L60
12	EC-Earth3-LR	Stockholm University, Europe	512 × 256, L91	362 × 292, L75
13	FGOALS-f3-L	Institute of Atmospheric Physics, CAS, China	288 × 180, L19	360 × 218, L30
14	FGOAS-g3	Institute of Atmospheric Physics, CAS, China	180 × 90, L26	360 × 218, L30
15	GISS-E2-1-G	NASA Goddard Institute for Space Studies, USA	144 × 90, L40	360 × 180, L32
16	MIROC-ES2L	Atmosphere and Ocean Research Institute, University of Tokyo, Japan	128 × 64, L40	360 × 256, L63
17	MPI-ESM1-2-LR	Max Planck Institute for Meteorology, Hamburg, Germany	192 × 96, L47	256 × 220, L40
18	MRI-ESM2-0	Meteorological Research Institute, Japan	320 × 160, L80	360 × 364, L61

Table 1. Basic information on the PMIP3/4 models adopted in this study. The first run is used if the model has multiple runs. The first 10 models are from the PMIP3 framework, and the last 8 models are from the PMIP4.

The mid-Holocene experiment sets the forcings at 6 ka BP and differs from the preindustrial control experiment mainly through orbital parameters (Table 2). The orbital configuration at the mid-Holocene is characterized by higher obliquity than at the preindustrial period, as well as perihelion closing to the boreal autumn equinox rather than boreal winter solstice as in today (Berger 1978), leading to differences in the seasonal and latitudinal distribution of the top-of-atmosphere insolation (Otto-Bliesner et al. 2017). The Northern Hemisphere features larger-than-present insolation from boreal late spring to early autumn, and for the Southern Hemisphere, the higher insolation occurs from boreal summer to autumn (Fig. 1). The atmospheric greenhouse gas (GHG) concentrations assigned to the mid-Holocene experiment are similar to those of the preindustrial control experiment, resulting in negligible changes in radiative forcing compared to the orbitally induced change (Otto-Bliesner et al. 2017; Brierley et al. 2020). Of note is that there are slight differences between the PMIP3 and PMIP4 experimental designs (Table 2), but they do not lead to considerable differences in the radiative forcing changes between the mid-Holocene and preindustrial period (Fig. 1c) (Otto-Bliesner et al. 2017; Brierley et al. 2020). In the meantime, the two phases of PMIP yield similar climate responses in the mid-Holocene (Brierley et al. 2020). As such, the analysis presented here is based on the multimodel ensemble from both phases, and the results for individual PMIP phases are provided in the supplementary materials. The multimodel mean is used to measure the central tendency of the collection of models. The model outputs are re-gridded commonly to a regular 1° × 1° horizonal resolution prior to further analyses.

Forcing and boundary conditions	**Preindustrial control**	**Mid-Holocene**
Orbital parameters	Eccentricity = 0.016724 / 0.016764 Obliquity = 23.446° / 23.459° Periapsis − 180° = 102.04° / 100.33°	Eccentricity = 0.018682 Obliquity = 24.105° Periapsis − 180° = 0.87°
Solar constant	1365 / 1360.747 W·m^{-2}	
Date of vernal equinox	March 21 at noon	
Greenhouse gases	CO_2 = 280 / 284.3 ppm CH_4 = 760 / 808.2 ppb N_2O = 270 / 273 ppb	CO_2 = 280 / 264.4 ppm CH_4 = 650 / 597 ppb N_2O = 270 / 262 ppb
Vegetation	Interactive vegetation or interactive carbon cycle or fixed to present day (depending on model complexity)	
Ice sheets	Modern	
Topography and coastlines	Modern	

Table 2. Experimental design for the preindustrial control and mid-Holocene experiments. More details on forcing and boundary conditions are available online at PMIP3 (https://pmip3.lsce.ipsl.fr/) and PMIP4 (https://pmip4.lsce.ipsl.fr/) websites. The values on the left and right of the slashes denote the designs of PMIP3 and PMIP4 experiments, respectively.

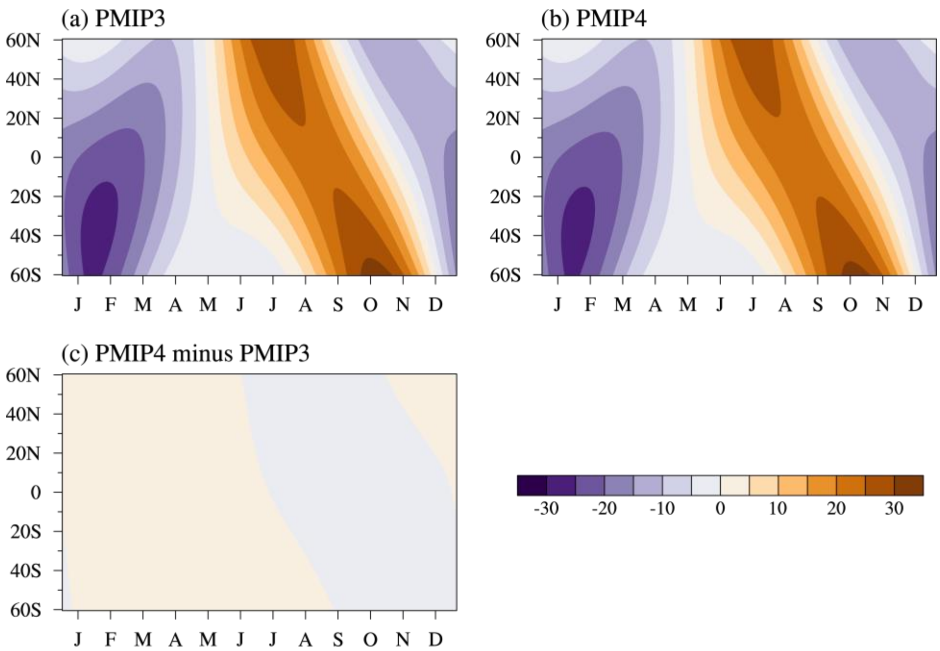

Fig. 1. Latitude–month sections of changes in incoming insolation at the top of atmosphere (W m^{-2}) between

the mid-Holocene and preindustrial periods in (a) PMIP3 and (b) PMIP4 protocols, as well as (c) their differences. The top-of-atmosphere insolation is calculated using modern calendar. The settings of orbital parameters are exhibited in Table 2.

The models' performance in simulating IOD characteristics is evaluated based on observed monthly SST from 1951 to 2000, which is taken from the National Oceanic and Atmospheric Administration Extended Reconstructed SST (ERSST) version 5 with a 2° × 2° horizontal resolution (Huang et al. 2017). As a comparison to the simulated change from the preindustrial period to the mid-Holocene, the proxy data that have been published in peer-reviewed journals are collected to depict the past climate condition around the IO (Table 3). The proxies documenting terrestrial moisture conditions include the speleothem oxygen isotope, mineral magnetic susceptibility, the hydrogen isotopic composition of leaf waxes, as well as the lake level inferred from paleo-shorelines. The earlier compilation of lake levels, the Global Lake Status Data Base (GLSDB) (Kohfeld and Harrison 2000), is also taken as a supplementary. The SST records collected here are mainly quantitative reconstructions based on Mg/Ca and alkenone palaeothermometry methods (Lohmann et al. 2013).

Location	**Lat**	**Lon**	**Proxy**	**Interpretation**	**Change**	**Reference**
Terrestrial Moisture						
Lake Chew Bahir	4.84	36.78	Magnetic susceptibility	Aridity	+	Foerster et al. (2012)
Lake Turkana	2.6	35.5	Paleo-shorelines	Lake level (Aridity)	+	Garcin et al. (2012)
Lake Suguta	2	36.5	Paleo-shorelines	Lake level (Aridity)	+	Garcin et al. (2009)
Mount Kenya	−0.15	37.35	Diatom silica $\delta^{18}O$	Aridity	+	Barker et al. (2001)
Lake Challa	−3.32	37.7	Leaf wax δD	Rainfall amount	+	Tierney et al. (2011)
Core SO189-144KL	1.226	98	Leaf wax δD	Annual rainfall	−	Niedermeyer et al. (2014)
SST over EEIO						
Core SO184-10043	−7.516	105.06	Alkenone	SST	–	Li et al. (2016b)
Core SO189-119KL	3.52	96.32	Mg/Ca ratios	SST	–	Mohtadi et al. (2014)
Core GeoB10029-4	−1.5	100.13	Mg/Ca ratios	SST	–	Mohtadi et al. (2010)
Core SK157-14	5.18	90.08	Mg/Ca ratios	SST	–	Raza et al. (2017)
Core SO139-74KL	−6.543	103.833	Alkenone	SST	–	Lückge et al. (2009)
SST over WEIO						
Core NIOP905	10.78	51.93	Alkenone	SST	−	Huguet et al. (2006)
Mahe´ and La Digue Island	−3 to −6	52 to 54	Sr/Ca ratios and $\delta^{18}O$	SST	Unchanged	Zinke et al. (2014)
Core GeoB12615-4	−7.14	39.84	Mg/Ca ratios	SST	Unchanged	Romahn et al. (2014)
Core MD900963	5.07	73.88	Alkenone	SST	−	Rostek et al. (1993)
Core 905	10.77	51.93	Mg/Ca ratios	SST	+	Anand et al. (2008)
Core MD85674	3.18	50.43	Alkenone	SST	+	Bard et al. (1997)

Table 3. Records documenting variations in terrestrial moisture and SST between the mid-Holocene and the present day. Latitudes and longitudes are expressed by the standard convention, with positive values for °N or °E and negative ones for °S or °W. The plus indicates wetter and warmer for moisture and SST records, respectively, while the minus denotes the opposite changes.

b. Identification of the IOD

Here, the difference in SST anomaly between the WEIO (50°E–70°E, 10°S–10°N) and the SEIO (90°E–110°E, 10°S–0°), referred to as Dipole Mode Index (DMI) (Saji et al. 1999), is taken to represent the IOD variability. Toward an extraction of interannual signals, a three-month running mean is performed to suppress the intraseasonal variability, and a nine-year running mean is subtracted to remove variations at decadal and longer timescales. The study considers the IOD intensity during the peak seasons August–November (ASON). The positive (negative) IOD events can be identified when the ASON DMI is greater (less) than 0.8 (−0.8) standard deviation. The intensity of IOD variability is measured based on two statistics: (1) the standard deviation of DMI and (2) the composite difference in DMI between positive and negative events. Likewise, the spatial distribution of the IOD-related climate is presented by a composite analysis as differences between positive and negative events. Furthermore, the thermocline is defined as the depth of the maximum vertical temperature gradient and is computed using a quadratic interpolation method.

Before the analysis, the models' ability to simulate IOD characteristics is assessed by comparing the simulation during the preindustrial period to the observation (Fig. 2). A key feature of the observed IOD is the pronounced seasonality with the peak season during ASON, which is demonstrated by the monthly standard deviation of the DMI (Fig. 2a). The multimodel mean reproduces the observed phase-locking feature notwithstanding an overestimation in the amplitude of IOD, which is a common bias for current climate models (Cai and Cowan, 2013). In terms of the spatial structure, the multimodel mean captures the IOD-related SST dipole pattern during the mature phase, although the simulated SST anomalies over the eastern pole extend farther west than the observation (Figs. 2b and c) as suffered by most coupled models (e.g., Liu et al. 2014; An et al. 2022). Note that it is impossible to obtain an identical pattern between the preindustrial simulation and the observation, partly because of the lower atmospheric GHG concentrations during the preindustrial period. Nevertheless, the comparison demonstrates that the multimodel ensemble is skillful in simulating major elements of IOD activities and is therefore reasonable to be used in the following analysis.

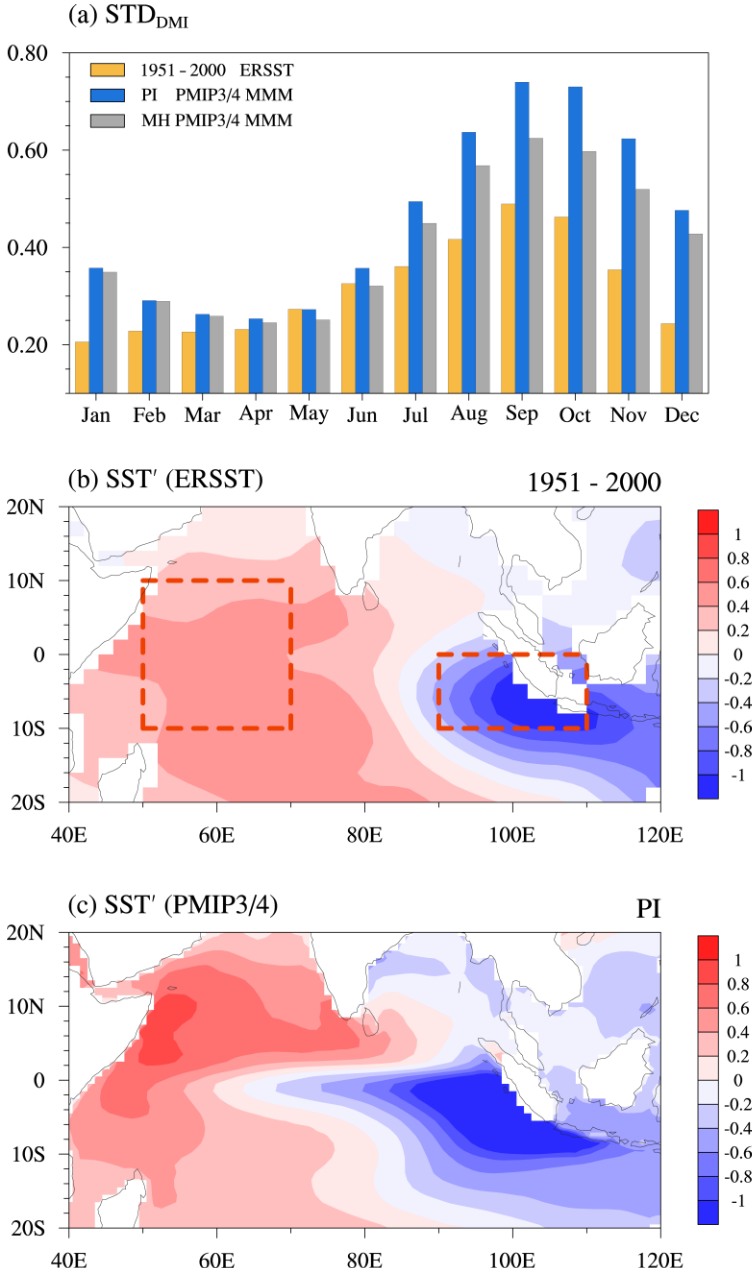

Fig. 2. (a) Comparison of IOD behaviors among the observation in the period 1951–2000 and the multimodel mean during the preindustrial period and mid-Holocene in terms of monthly standard deviation of DMI. The IOD composite SST anomalies during ASON based on (b) the observation and (c) preindustrial control experiment. The red boxes in (b) indicate the WEIO and SEIO zones for computing DMI.

c. Mixed-layer heat budget

Generally, the SST anomaly is determined by both surface heat fluxes and oceanic dynamics. To investigate why IOD-related SST anomalies differ between the two periods, we quantify the relative roles of the dynamic and thermodynamic processes through decomposing the MLHB equation. In this equation, the mixed-layer-averaged temperature tendency can be written as follows (Li et al. 2002):

$$
\begin{aligned}
\frac{\partial T'}{\partial t} &= -\left\langle \mathbf{V}\cdot\nabla T\right\rangle' + \frac{Q'_{\text{net}}}{\rho_0 C_p H} + r \\
&= -\left\langle \mathbf{V}'\cdot\nabla\bar{T} + \bar{\mathbf{V}}\cdot\nabla T' + \mathbf{V}'\cdot\nabla T'\right\rangle + \frac{Q'_{\text{net}}}{\rho_0 C_p H} + r \\
&= -\left\langle w'\frac{\partial\bar{T}}{\partial z} + \bar{w}\frac{\partial T'}{\partial z} + w'\frac{\partial T'}{\partial z}\right\rangle - \left\langle v'\frac{\partial\bar{T}}{\partial y} + \bar{v}\frac{\partial T'}{\partial y} + v'\frac{\partial T'}{\partial y}\right\rangle - \left\langle u'\frac{\partial\bar{T}}{\partial x} + \bar{u}\frac{\partial T'}{\partial x} + u'\frac{\partial T'}{\partial x}\right\rangle + \frac{Q'_{\text{net}}}{\rho C_p H} + r
\end{aligned}
\tag{1}
$$

where T is the mixed-layer-averaged temperature, $\mathbf{V} = (u, v, w)$ denotes the three-dimensional flow velocity, $\nabla = (\partial/\partial x, \partial/\partial y, \partial/\partial z)$ is a three-dimensional gradient operator; Q_{net} indicates the net surface heat flux (downward positive), which is the sum of net downward longwave, shortwave, sensible heat, and latent heat fluxes; ρ and C_p represent seawater density and specific heat (4000 J kg K^{-1}), respectively; H denotes the mixed-layer depth where the ocean temperature is 0.5 °C lower than SST (Li et al. 2002); r represents the residual term due to entrainment, diffusion, etc. The overbar denotes the climatological monthly mean, the prime denotes the departure from it, and the angle bracket indicates the vertical integration from the ocean surface to bottom of the mixed layer. Here, the term $-\mathbf{V}'\cdot\nabla\bar{T}$ indicates the advection by anomalous currents acting on the mean-state temperature gradient, and $-\bar{\mathbf{V}}\cdot\nabla T'$ represents the advection by mean-state currents acting on the anomalous temperature gradient. The mixed-layer integration of the vertical advection reflects the net effect at the bottom of the mixed layer. Hereafter, the change between the mid-Holocene and preindustrial periods are marked by Δ. For example, the change in the mixed-layer temperature tendency is represented by $\Delta\frac{\partial T'}{\partial t}$.

3. Changes in the mean state

a. Results from the simulation

Compared to the preindustrial period, the top-of-atmosphere insolation during the mid-Holocene increases in the Northern Hemisphere from May to September and enhances in the Southern Hemisphere during June–November (Fig. 1). The surface of the Earth is correspondingly warmed with an approximate one-month lagging behind the insolation change on land and two months over the ocean (not shown). Given that terrestrial soil has a much smaller heat capacity than ocean water, land warms more severely than the ocean, amplifying the land–ocean thermal contrast in the Northern Hemisphere during the boreal summer and in the Southern Hemisphere during the boreal autumn (Figs. 3a and b).

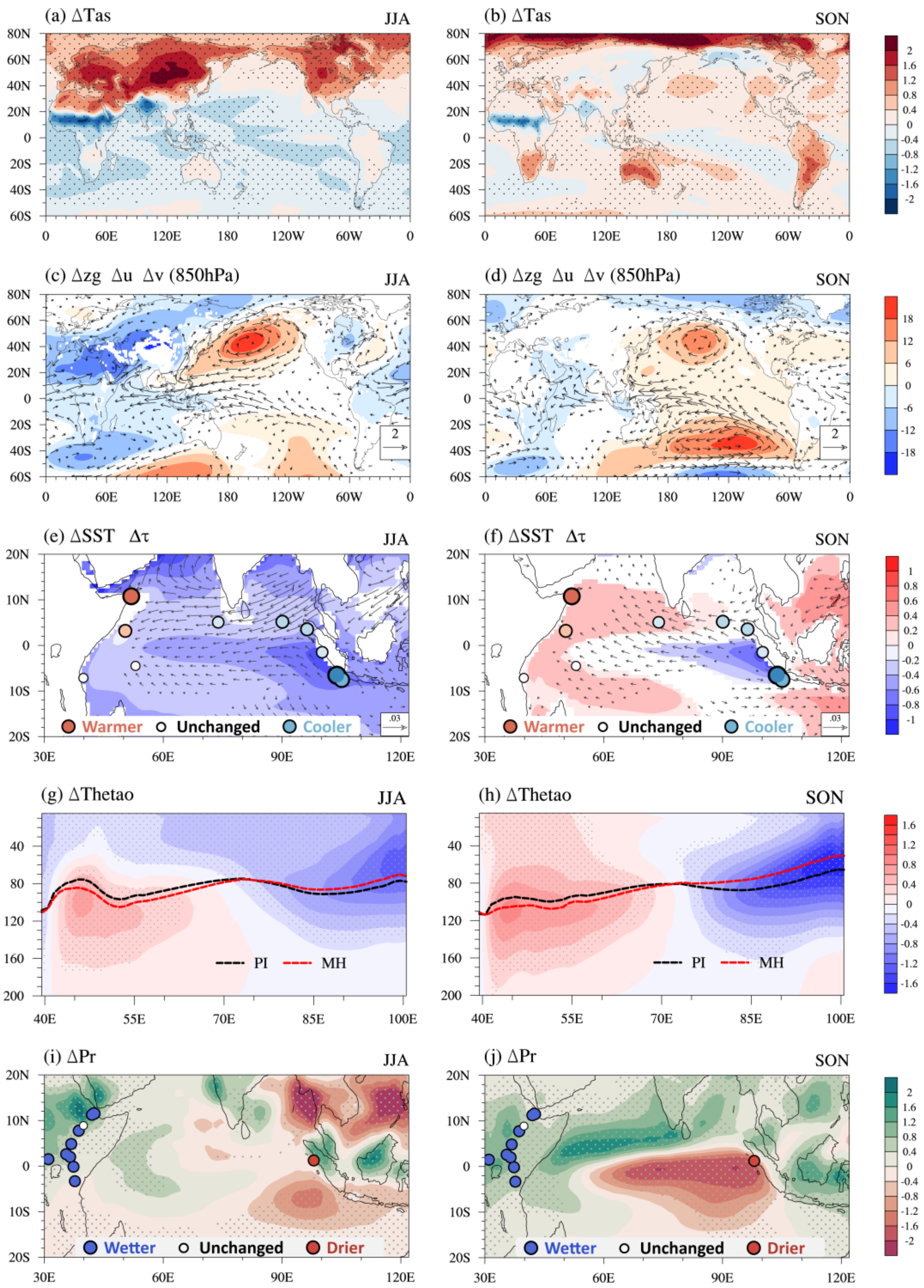

Fig. 3. The mid-Holocene minus preindustrial period difference in (a–b) near-surface air temperature (°C), (c–d) 850-hPa geopotential height (m) and horizontal winds (m s^{-1}), (e–f) SST (°C) and wind stress (Pa), (g–h) seawater potential temperature (°C), as well as (i–j) precipitation (mm day^{-1}) during JJA (left column) and SON (right column). In (c–f), only the significant change at the 95% confidence level is shown; for other panels, the significant change is marked with stippling. Red and black lines for (g–h) indicate the positions of thermoclines during the mid-Holocene and preindustrial period, respectively. The circles in (e–f) are proxy-based SST reconstructions (Table 3), with larger ones representing greater changes compared to the present day. The circles in (i–j) are qualitative records (Table 3) implying terrestrial moisture changes. Note that the proxies in the left and right columns are the same.

Over the equatorial IO, in addition to the insolation forcing, the temperature change depends largely on the alteration in regional circulations. As manifested in the 850-hPa circulation field (Figs. 3c and d), the strengthening land–sea thermal contrast deepens the North and South Pacific subtropical anticyclones (He and Zhou 2020), inducing enhanced equatorial easterlies across the Indo–Pacific from boreal summer to autumn when IOD grows. This result is in accordance with the previous simulation that reported a strengthening and westward shift of the Pacific Walker circulation (Tian et al. 2018). As a response to such an easterly wind change, the equatorial IO features a positive IOD-like variation in SST and precipitation (Figs. 3e–j). Specifically, compared to the preindustrial period, there appear enhanced westward wind stress across the equatorial IO and northwestward wind stress over the SEIO throughout the boreal summer and autumn. Correspondingly, the SEIO is significantly cooler with decreased precipitation and shoaling thermocline; the WEIO is characterized by less severe JJA cooling compared to the SEIO and even warming during the SON, accompanied by increased precipitation and deepened thermocline.

b. Results from paleo-data

The simulated positive IOD-like change in the basic-state SST and precipitation is also registered by geological evidence (Table 3). This study collects a set of marine sediment records that quantitatively reconstruct SST changes between the mid-Holocene and the present day (Figs. 3e and f). Five records to the west of the Sumatra Island document an SST decrease that ranges from −0.2 to −0.7 °C, with an average of −0.4 °C. In the WEIO, 2 out of 6 records indicate that SST is 0.2 to 0.4 °C below the present day, and other records show that SST is rarely changed or increased. By comparison, the change in the WEIO is more moderate than that in the EEIO, indicating a negative zonal gradient in the SST change across the equatorial IO. Such a negative gradient of SST change is also reported in previous complications of a few paleoclimatic records (Cui et al. 2022; Weldeab et al. 2022). It should be noted that the paleorecords largely reflect signals of annual mean rather than that during IOD growing seasons. Nonetheless, the simulation coincides with the records, as there is also a negative gradient of the simulated annual-mean SST change (Fig. 4a), with larger-than-0.5 °C cooling in the EEIO and less-than-0.1 °C cooling in the WEIO. Such a negative gradient of the annual-mean SST change is mostly formed in the boreal summer and autumn when IOD grows (Fig. 4b).

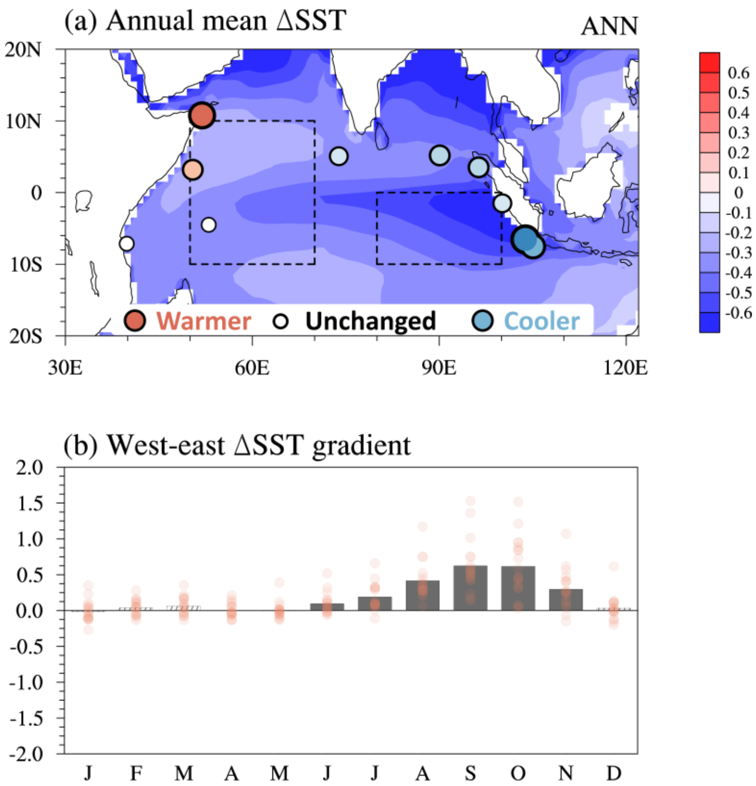

Fig. 4. The mid-Holocene minus preindustrial period difference in (a) annual mean SST and (b) monthly mean west–east SST gradient. In (a), only the change significant at the 95% confidence level is shown; the circles are the proxy-based SST reconstructions that are the same as in Figs. 3e–f. In (b), the west–east gradient is defined as the difference between the western (50°E–70°E, 10°S–10°N) and eastern (80°E–100°E, 10°S–0°) IO zones (black boxes in a); the bars indicate multimodel mean changes with grey filling denoting significance at the 95% confidence level; the red circles represent changes in each model.

In addition, the IOD-like response in precipitation is exhibited in a set of hydroclimatic records (Figs. 3i and j). It should be noted first that considering the leading role of precipitation in terrestrial moisture change during the mid-Holocene (Liu et al. 2019), the proxy-inferred alteration in land moisture can be regarded as an implication of the precipitation change. As such, the proxies over eastern Africa, including larger magnetic susceptibility (Foerster et al., 2012), higher lake levels inferred from paleo-shorelines (Kohfeld and Harrison 2000; Garcin et al. 2009; Garcin et al. 2012), lighter $\delta^{18}O$ of diatom silica (Barker et al. 2001), and lighter δD of leaf waxes (Tierney et al. 2011), indicate an increase in precipitation compared to the present day, while the heavier δD of leaf waxes (Niedermeyer et al. 2014) over equatorial West Sumatra reflects precipitation reduction. Note second that although the paleo-records are not located in the core IOD region, they are from regions with a close relationship between precipitation and IO SST. Over eastern equatorial Africa, the WEIO warming could favor precipitation through the delivery of high moist static energy air into the land, and this process acts to form two rainy seasons during March–May and October–December (Yang et al. 2015). The equatorial West

Sumatra locates within the equatorial rainfall regime, which is modulated by IO SST and less affected by monsoons (Niedermeyer et al. 2014). Accordingly, the reconstructed change in precipitation can to a large extent reflect the change in SST.

4. Changes in the IOD variability

a. Variance and composite structures

Compared to the preindustrial period, the IOD in the mid-Holocene weakens across the growing and mature seasons as represented by reduced standard deviations of DMI (Fig. 2a). For the peak season ASON, 12 out of 18 models consistently simulate a decrease in the DMI standard deviation, with a 14% decrease shown in the multimodel mean (Fig. 5a). Such a reduction in the DMI standard deviation reveals a weakening of IOD variability. The spatial structure of the IOD-related SST is presented by the SST differences between the composite positive and negative events (Fig. 6). Compared to the preindustrial period, the IOD-induced WEIO warming during the mid-Holocene declines by 40% in the multimodel mean, and 13 out of 18 models agree on the sign of the change (Fig. 6c); for the SEIO, however, the change is not significant with substantial discrepancies across models (Fig. 6c). Accordingly, the declination of WEIO SST variability dominates the weakening of IOD variability.

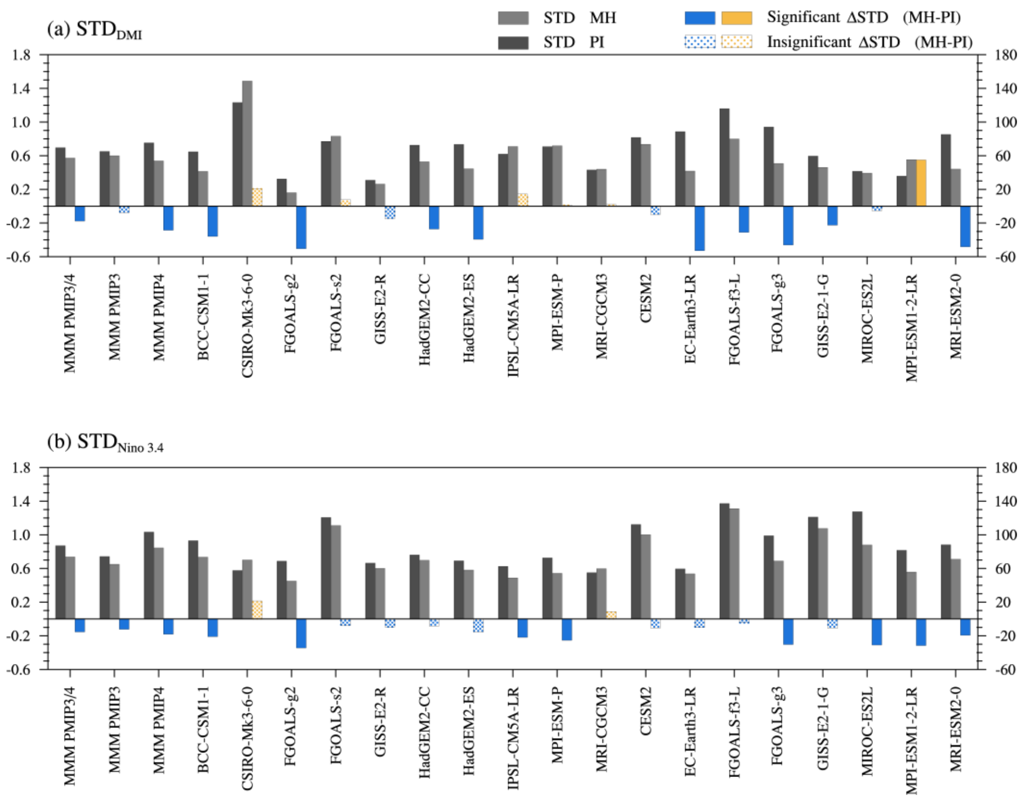

Fig. 5. Standard deviations of (a) DMI and (b) Niño-3.4 SST index during ASON for the preindustrial period (dark gray bars; left *y* axis) and mid-Holocene (light gray bars; left *y* axis), as well as the percentage change

(%) from the preindustrial period to mid-Holocene (yellow and blue bars; right y axis). The color-filled/dotted bar indicates the change above/below the 95% confidence level.

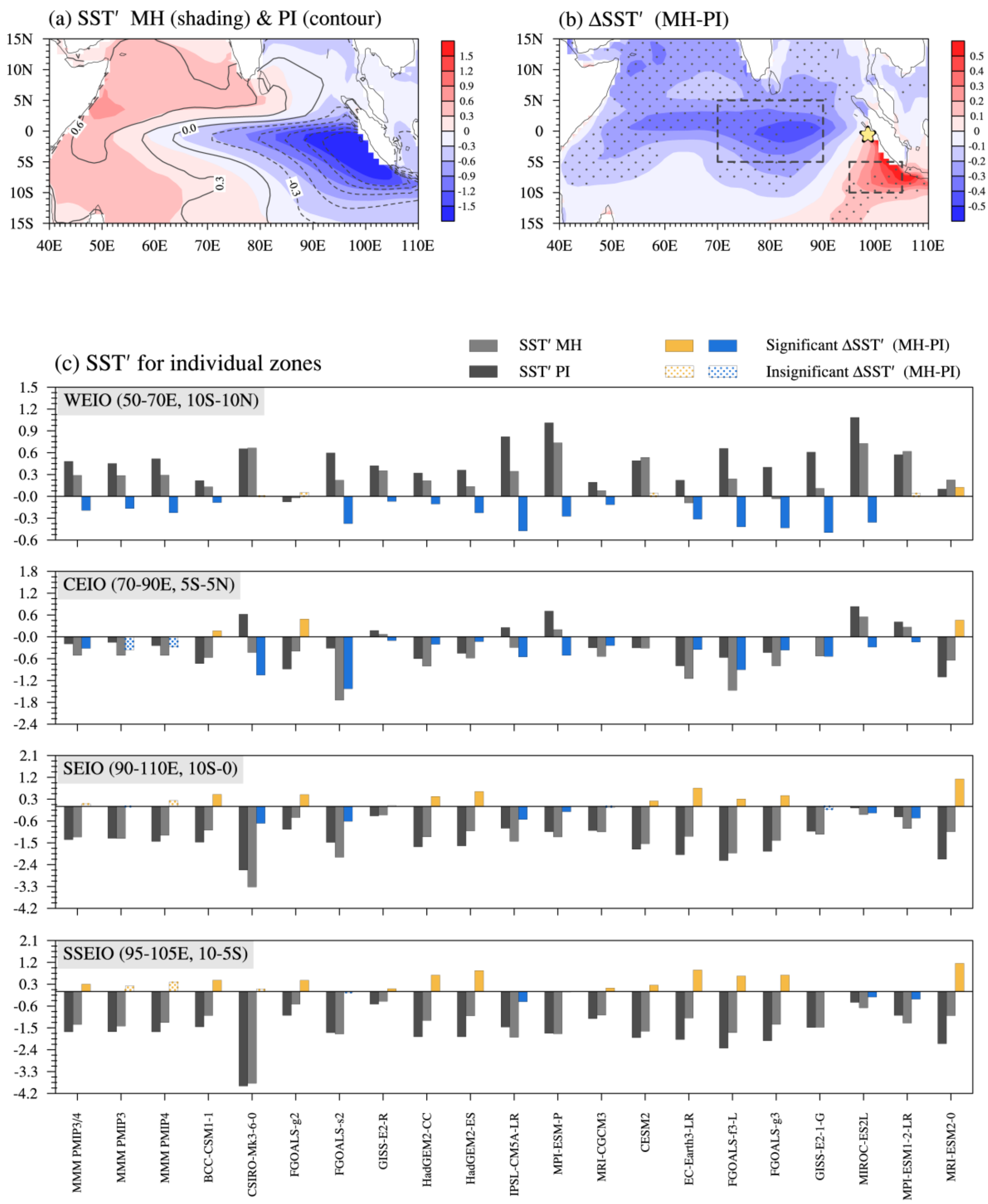

Fig. 6. Spatial distribution of IOD composite SST anomalies (SST′) during ASON for (a) the preindustrial period (contour, °C) and mid-Holocene (shading, °C) and (b) the change between the two periods (ΔSST′). (c) The regional averages of SST′ and ΔSST′ for the WEIO, CEIO, SEIO, and SSEIO. In (b), the stippling indicates regions where the change is statistically significant at the 95% confidence level, the yellow star marks the coral record station from the Mentawai Islands (Abram et al. 2007), and the black boxes denote the CEIO and SSEIO zones. The color-filled/dotted bars in (c) indicate the change above/below the 95% confidence level.

Notwithstanding the negligible change regarding the SEIO regional mean, the southern corner of SEIO (SSEIO, 95°E–105°E, 10°S–5°S) features that the IOD-related SST cooling is 18% below that during the preindustrial period, with 13 out of 18 models agreeing on the sign of the change. Such a change indicates a northward contraction of the eastern cooling pole. It is also revealed that the eastern cooling pole extends westward compared to the preindustrial period (Figs. 6a and b), leading to 61% more cooling over the central equatorial IO (CEIO, 70°E–90°E, 5°S–5°N) according to the multimodel mean (Fig. 6c). There are 14 out of 18 models agreeing on the sign of such a change in CEIO, suggesting prominent consistency across models. Overall, the aforementioned dipole SST change indicates a slight northwestward shift of the eastern cooling pole.

A coral-based reconstruction from the Mentawai Islands (Fig. 6b) provides evidence of IOD-related SST changes off the Sumatra coast (Abram et al. 2007). The reconstruction captures four positive IOD events at the mid-Holocene, which are characterized by similar magnitudes of IOD SST cooling compared to the four events at the late Holocene (Abram et al. 2007). As shown by the yellow star in Fig. 6b, the location of the reconstruction resides right between the simulated dipole SST changes and thus is barely affected by the change in the simulation. Therefore, the simulation coincides with the reconstruction at this region.

Of note is that there are total 30 PMIP3/4 models that published the outputs of the mid-Holocene simulations. Although the present analysis is based on an 18-model subset due to the availability of variables, the results in terms of the amplitude and spatial structure also hold for the multimodel means of the total 30 models (Fig. S2). Furthermore, the results based on mere PMIP3 or PMIP4 models are also similar (Figs. S2 and S3).

b. Mixed-layer heat budget

Toward addressing the causes of the IOD change, an MLHB analysis is conducted to diagnose the mixed-layer temperature anomaly (MLTA) tendency of the composite IOD events during the growing phase (May–October). The analysis focuses on the WEIO, CEIO, and SSEIO where changes are statistically significant. Figure 7 shows the change from the preindustrial period to the mid-Holocene in the MLTA tendency and the contributions of individual terms. It is shown that the actual MLTA tendency (Fig.7, bars 1) can be reasonably approximated by the sum of advection and heat flux terms (Fig.7, bars 2), so the MLTA tendency change can be elucidated by comparing individual terms of the equation. In the WEIO, the MLTA tendency reduces significantly compared to the preindustrial period (Fig. 7a), responsible for the damped amplitude of the IOD-induced warming. The reduction in MLTA tendency can be largely attributed to the negative change in advection terms. Among them, $-\Delta(\bar{u}\frac{\partial T'}{\partial x})$, $-\Delta(u'\frac{\partial \bar{T}}{\partial x})$, and $-\Delta(\bar{v}\frac{\partial T'}{\partial y})$ are the dominant contributors significant at the 95% confidence level. In particular, $-\Delta(\bar{u}\frac{\partial T'}{\partial x})$ is at least 1.6 times the magnitude of the other two terms and thus serves as the leading factor in the attenuation of IOD-induced warming over the WEIO. Over the CEIO (Fig. 7b), the negative change in MLTA tendency can be attributed to the significant decrease in $-\Delta(\bar{u}\frac{\partial T'}{\partial x})$ and $-\Delta(v'\frac{\partial \bar{T}}{\partial y})$, and the former is 1.1 times larger than the later. For the SSEIO sector (Fig. 7d), $-\Delta(\bar{v}\frac{\partial T'}{\partial y})$, $-\Delta(v'\frac{\partial \bar{T}}{\partial y})$, and $-\Delta(\bar{w}\frac{\partial T'}{\partial z})$ are distinguished as main terms responsible for the weakening of the negative MLTA tendency, accounting for the suppressed SST anomalies linked to the IOD. Of note is that although the former two terms are insufficiently significant because of a large intermodel spread, there is a substantial intermodel agreement on the sign.

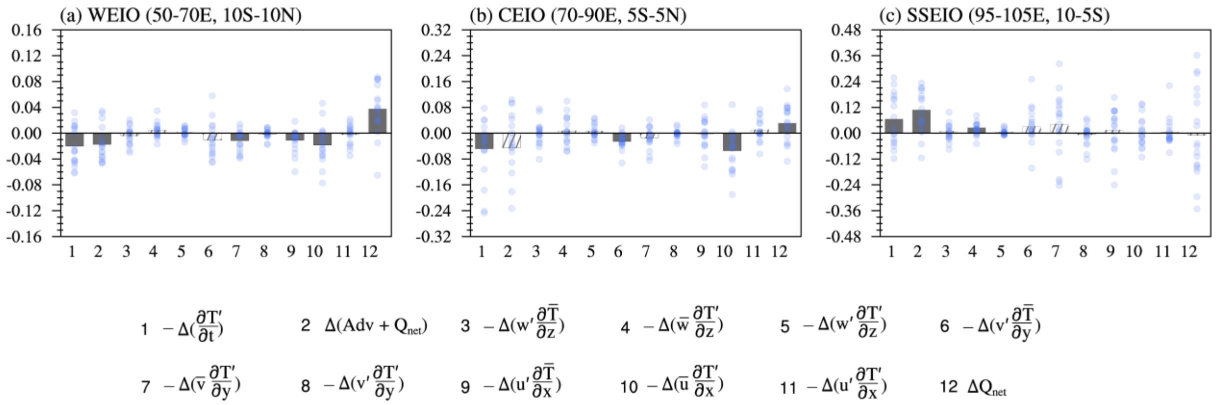

Fig. 7. The mid-Holocene minus preindustrial period difference in IOD composite anomalies of mixed layer heat budget terms during MJJASO over the (a) WEIO, (b) CEIO, and (c) SSEIO. The bars indicate the multimodel means with grey-filling/striping denoting the significance above/below the 95% confidence level, and the blue circles represent individual models.

Given that the aforementioned contribution terms are formed as products of the mean state and IOD-induced perturbation, a further decomposition is conducted to elucidate the relevant importance of the change in the mean state or perturbation (Fig. 8). The equation can be written as follows:

$$\Delta(A'\bar{B}) = A'(\Delta\bar{B}) + (\Delta A')\bar{B} + (\Delta A')(\Delta\bar{B}) \qquad (2)$$

where Δ indicates the difference between the mid-Holocene and preindustrial periods; A' and

$\bar{B}$ denote the perturbation (e.g., $-\frac{\partial T'}{\partial x}$ and u') and basic state (e.g., $-\frac{\partial \bar{T}}{\partial x}$ and $\bar{u}$) parts, respectively. The term $A'(\Delta\bar{B})$ measures the effects of the climatological mean-state change, and $(\Delta A')\bar{B}$ represents the contributions of changes in the IOD-induced perturbations. Note that in this analysis, the mixed-layer depth is fixed at the preindustrial climatological level, because its change during the mid-Holocene is limited and thus not taken into account.

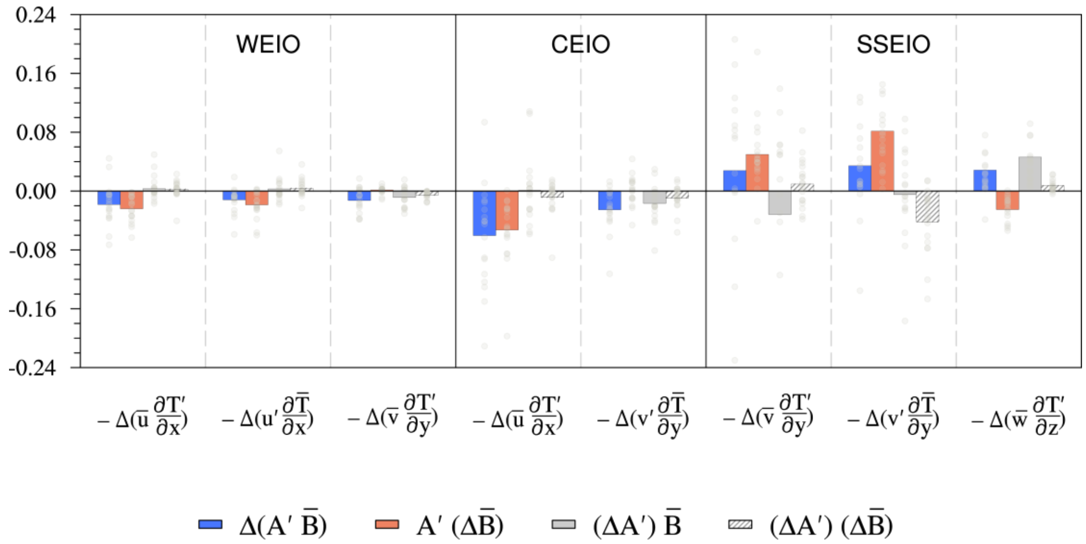

Fig. 8. Separate contributions of the changes in the basic state (orange bars; $A'(\Delta\bar{B})$), perturbation (gray bars; $(\Delta A')\bar{B}$), or both (striped bars; $(\Delta A')(\Delta\bar{B})$) to the changes of mixed layer heat budget terms (blue bars; $\Delta(A'\bar{B})$). Results for individual models are marked with gray circles.

Over the WEIO, the mean state component $-(\Delta\bar{u})\frac{\partial T'}{\partial x}$ greatly approximates $-\Delta(\bar{u}\frac{\partial T'}{\partial x})$, while other components are remarkably small (Fig. 8), meaning that the change in the background zonal current is the dominant factor in $-\Delta(\bar{u}\frac{\partial T'}{\partial x})$. As a further examination from the spatial perspective, the map of the mixed-layer integration and vertical profile of the equatorial mean are presented (Figs. 9a and b). The result confirms the dominant role of $-(\Delta\bar{u})\frac{\partial T'}{\partial x}$, which nearly reconstructs the horizontal and vertical structures of $-\Delta(\bar{u}\frac{\partial T'}{\partial x})$ in the WEIO (Fig. 9a). This result can be physically explained. As shown in Fig. 9b, the positive IOD event corresponds to a widespread negative zonal gradient of temperature anomalies ($\frac{\partial T'}{\partial x} < 0$) throughout the mixed layer; in the meantime, the enhancement of the basic-state easterly wind stress (Figs. 3e and f) drives a westward change in the mixed-layer zonal current ($\Delta\bar{u} < 0$).

Ultimately, $-(\Delta\bar{u})\dfrac{\partial T'}{\partial x}$ is negative, indicating an enhanced inflow of perturbation cold water by mean zonal currents from the eastern cooling pole. To the term $-\Delta(u'\dfrac{\partial \bar{T}}{\partial x})$, the mean state part $-u'(\Delta\dfrac{\partial \bar{T}}{\partial x})$ is also the most important contributor (Fig. 8), showing a similar magnitude and spatial distribution to that of $-\Delta(u'\dfrac{\partial \bar{T}}{\partial x})$ (Fig. 9c), while other components are negligible. As has been exhibited in the previous section, the mid-Holocene IO mean state has a positive IOD-like change in temperature compared to the preindustrial period (Figs. 3e–h), causing a decreased zonal gradient of the basic-state temperature ($\Delta\dfrac{\partial \bar{T}}{\partial x}<0$, Fig. 9d) and ultimately declined thermal advection by IOD easterly current anomalies from the Indian Ocean Warm Pool. In terms of the third term $-\Delta(\bar{v}\dfrac{\partial T'}{\partial y})$, the change in the meridional perturbation temperature gradient ($\Delta\dfrac{\partial T'}{\partial y}$) is dominant (Fig. 8). Compared to the preindustrial period, the western warming pole of the positive IOD shifts less northward in the mid-Holocene (Fig. 6a). This leads to a negative difference in the meridional gradient of SST anomalies ($\Delta\dfrac{\partial T'}{\partial y}<0$) and thus the negative difference in the meridional advection by the climatological southward surface current, which is induced by the summer monsoon-related Ekman transport ($-\Delta(\bar{v}\dfrac{\partial T'}{\partial y})<0$) (Schott et al. 2009).

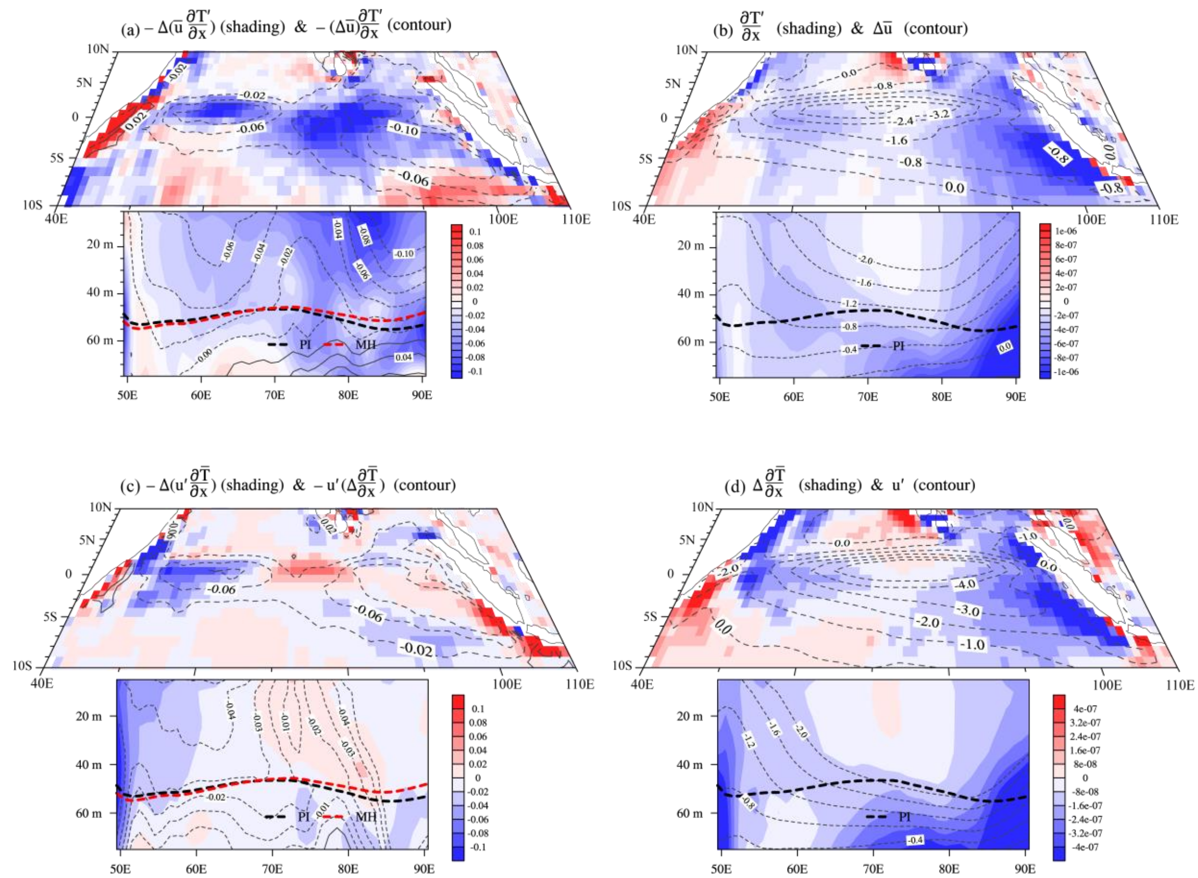

Fig. 9. The mixed-layer integrated map (top plot for each panel) and vertical profile of equatorial mean (5°S–5°N, bottom plot for each panel) of the changes in MLHB terms and their main contributors. (a) $-\Delta(\bar{u}\dfrac{\partial T'}{\partial x})$ (shading; °C mon^{-1}) and $-(\Delta\bar{u})\dfrac{\partial T'}{\partial x}$ (contour; °C mon^{-1}), which is further decomposed into (b) $\dfrac{\partial T'}{\partial x}$ during the preindustrial period (shading; °C m^{-1}) and $\Delta\bar{u}$ (contour; 10^5 m mon^{-1}). (c) $-\Delta(u'\dfrac{\partial \bar{T}}{\partial x})$ (shading; °C mon^{-1}) and $-u'(\Delta\dfrac{\partial \bar{T}}{\partial x})$ (contour; °C mon^{-1}), which can be decomposed into (d) $\Delta\dfrac{\partial \bar{T}}{\partial x}$ (shading; °C mon^{-1}) and preindustrial period u' (contour; 10^5 m mon^{-1}). Red and black dashed bold lines indicate the bottom of the mixed layer during the mid-Holocene and preindustrial period, respectively.

Concerning the CEIO, the primary mechanism behind the strengthening of the MLTA tendency is the same as that in the WEIO, that is, the enhanced inflow of perturbation cold water by mean zonal currents from the eastern pole ($-(\Delta\bar{u})\dfrac{\partial T'}{\partial x} < 0$). The secondary factor $-\Delta(v'\dfrac{\partial \bar{T}}{\partial y})$ is caused by a change in the IOD-related perturbation of the meridional currents ($\Delta v'$) (Fig. 8), and the perturbation component $-(\Delta v')\dfrac{\partial \bar{T}}{\partial y}$ sufficiently reproduces the full term

$-\Delta(v'\frac{\partial \overline{T}}{\partial y})$ across the mixed layer (Fig. 10a). Generally, during positive IOD events, the westward wind stress perturbation appears over the tropical IO (Fig. 11a), driving anomalous Ekman flows (v') northward/southward over the Northern/Southern Hemisphere (Fig. 10c). Such anomalous Ekman flows act to spread the equatorial heat poleward, suppressing the westward extension of the eastern cooling pole (Figs. 10b and c). Compared to the preindustrial period, the IOD-related Ekman flows are weakened (Fig. 10b) because of the subdued zonal wind stress perturbation (Fig. 11b). Ultimately, warm water transporting away from the equator is below the preindustrial period, accounting for the decreased MLTA tendency over the CEIO. Furthermore, the subdued zonal wind stress perturbation is a response to the change in IOD-induced anomalies in SST (Fig. 6b) and precipitation (Fig. 11b), indicating the close air–sea coupling in the tropical IO.

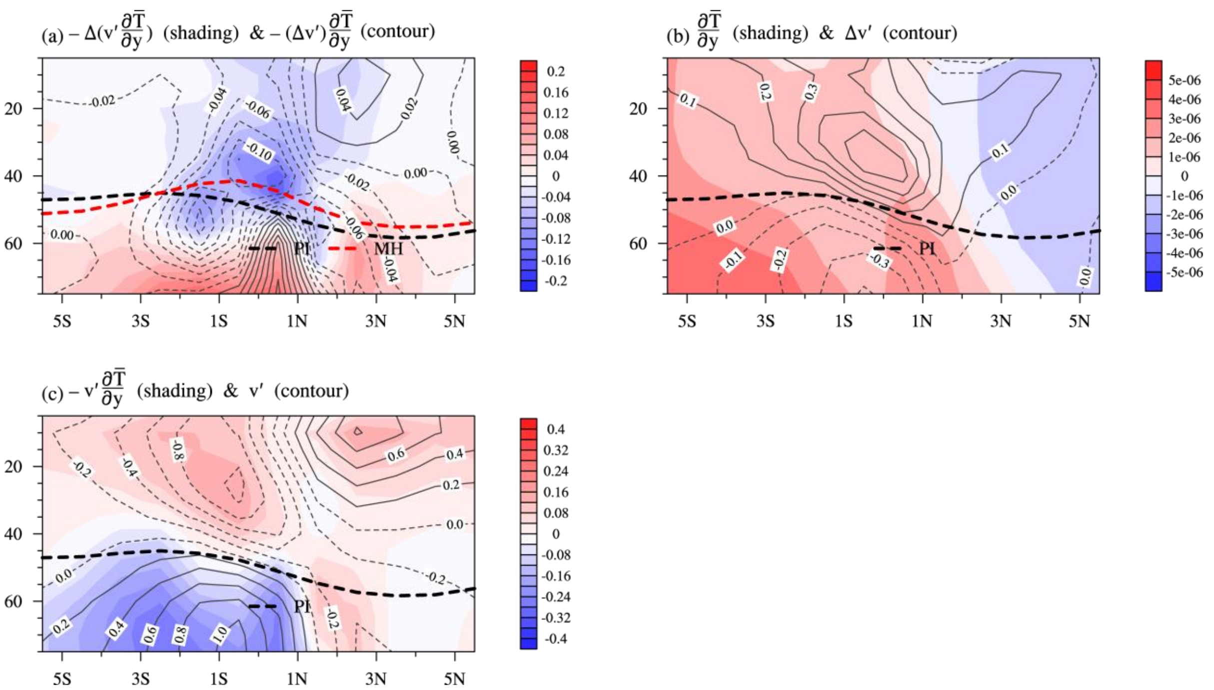

Fig. 10. The vertical profile of 70°E–90°E averaged (a) $-\Delta(v'\frac{\partial \overline{T}}{\partial y})$ (shading; in the unit of °C mon^{-1}) and $-(\Delta v')\frac{\partial \overline{T}}{\partial y}$ (contour; °C mon^{-1}), which is further decomposed into (b) $\frac{\partial \overline{T}}{\partial y}$ at the preindustrial period (shading; °C m^{-1}) and $\Delta v'$ (contour; 10^5 m mon^{-1}), as well as (c) preindustrial period terms $-v'\frac{\partial \overline{T}}{\partial y}$ (shading; °C mon^{-1}) and v' (contour; 10^5 m mon^{-1}).

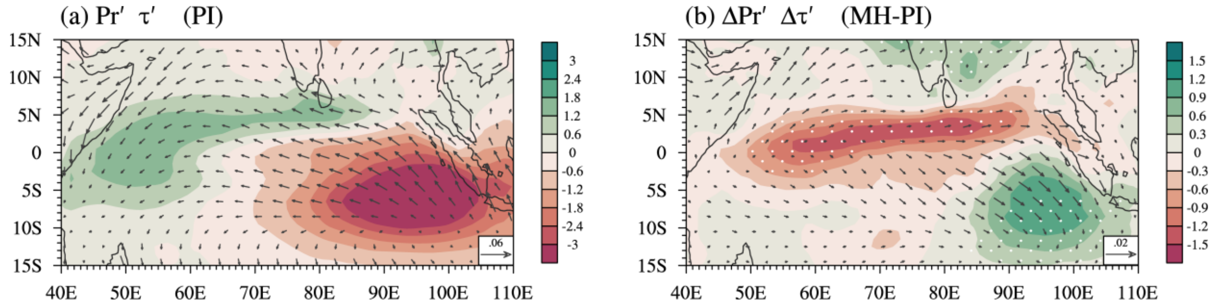

Fig. 11. Spatial distribution of IOD composite anomalies in precipitation (mm day^{-1}) and wind stress (Pa) during MJJASO for (a) the preindustrial period (Pr′ and τ′) and (b) the change from the preindustrial period to the mid-Holocene (ΔPr′ and Δτ′). Stippling in (b) indicates regions where the precipitation change is statistically significant at the 95% confidence level.

In the SSEIO, the result indicates that both the positive $-\Delta(\bar{v}\frac{\partial T'}{\partial y})$ and $-\Delta(v'\frac{\partial \bar{T}}{\partial y})$ arise from the mean-state alterations (Fig. 8); the spatial patterns of $-\Delta(\bar{v}\frac{\partial T'}{\partial y})$ and $-\Delta(v'\frac{\partial \bar{T}}{\partial y})$ can be reasonably replicated by $-(\Delta\bar{v})\frac{\partial T'}{\partial y}$ (Fig. 12a) and $-v'(\Delta\frac{\partial \bar{T}}{\partial y})$ (Fig. 12c), respectively. To be specific, the enhancement of the basic-state southeastward wind stress (Fig. 3e) drives increased northward flows ($\Delta\bar{v} > 0$, Fig. 12b) that accelerate the northward mean advection of IOD perturbations, leading to positive $-(\Delta\bar{v})\frac{\partial T'}{\partial y}$. In addition, positive IOD-like change in the mean-state temperature causes a decreased meridional temperature gradient ($\Delta\frac{\partial \bar{T}}{\partial y} < 0$, Fig. 12d) and ultimately declined thermal advection by IOD northward current perturbations. Furthermore, the positive $-\Delta(\bar{w}\frac{\partial T'}{\partial z})$ arises from the perturbation term (Fig. 8). Normally, when positive IOD events occur, the anomalous equatorial easterlies generate poleward mass transport in both hemispheres and subsequently surface divergence, which propagates eastward as upwelling Kelvin waves and shoals the thermocline. The thermocline shoaling corresponds to subsurface cooling, which is delivered to the surface by basic-mean upwelling flows. Compared to the preindustrial period, the weakened easterly wind perturbation (Fig. 11b) partially suppresses this process and leads to positive $-\Delta(\bar{w}\frac{\partial T'}{\partial z})$.

As shown above, the dominant terms responsible for the weakened IOD can be largely tracked back to the mean-state change, which is characterized by the positive-IOD like pattern. This suggests a controlling role of the mean state on the IOD variability.

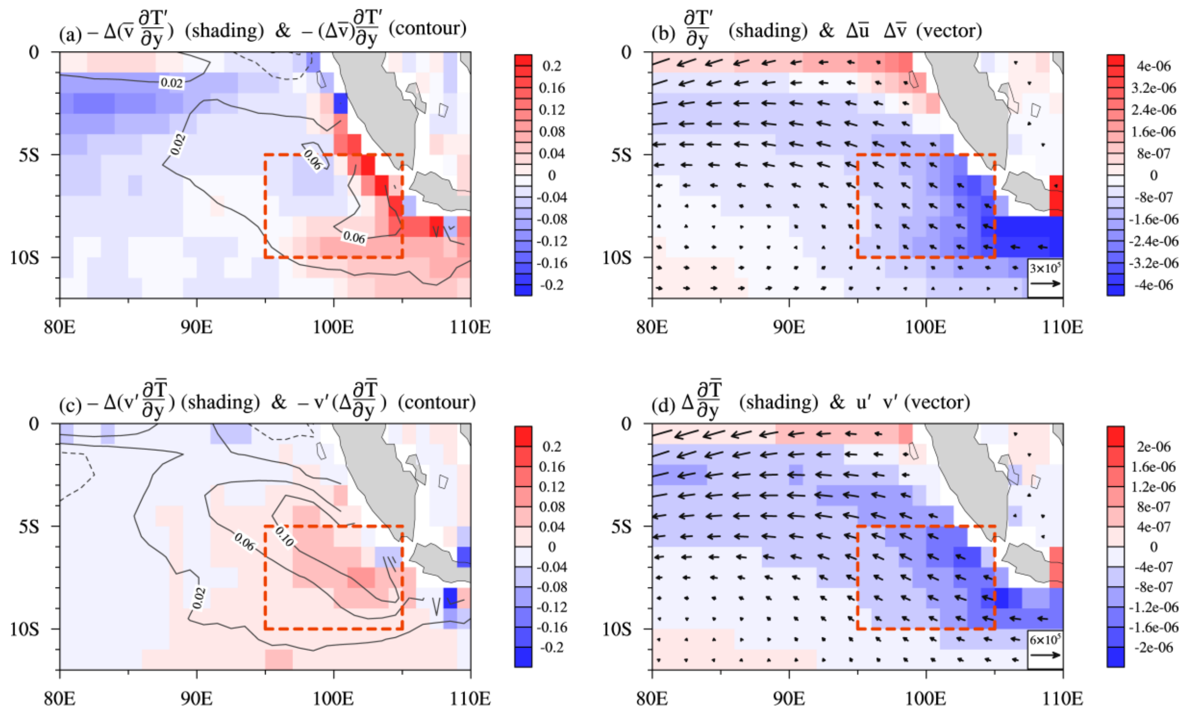

Fig. 12. The map of the mixed-layer integrated changes in MLHB terms and their main contributors. (a) $-\Delta(\bar{v}\frac{\partial T'}{\partial y})$ (shading; °C mon^{-1}) and $-(\Delta\bar{v})\frac{\partial T'}{\partial y}$ (contour; °C mon^{-1}), which is further decomposed into (b) $\frac{\partial T'}{\partial y}$ during the preindustrial period (shading; °C m^{-1}) and $\Delta\bar{v}$ (vector; m mon^{-1}). (c) $-\Delta(v'\frac{\partial \bar{T}}{\partial y})$ (shading; °C mon^{-1}) and $-v'(\Delta\frac{\partial \bar{T}}{\partial y})$ (contour; °C mon^{-1}), which can be decomposed into (d) $\Delta\frac{\partial \bar{T}}{\partial y}$ (shading; °C mon^{-1}) and preindustrial period v' (vector; m mon^{-1}). The boxes in (c–d) denote the SSEIO.

c. Relationship between changes in ENSO and IOD

ENSO is an important external forcing of the IOD activity. It has been documented that positive IOD events tend to co-occur with El Niño, which can affect the tropical IO by disturbing the Walker circulations and Indonesian Throughflow (Zhang et al. 2015; Stuecker et al. 2017; Cai et al. 2019). Here, the Niño-3.4 index (Rasmusson and Carpenter 1982), namely the area average of SST anomalies over 5°N–5°S and 170°W–120°W, is taken to identify the canonical ENSO. It is shown that the simultaneous correlation coefficient between the ASON DMI and Niño-3.4 index is 0.44 during the preindustrial period as indicated by the multimodel mean, which is very close to the observed 0.45 based on ERSST. At the same time, the multimodel mean reasonably reproduces the observed large-scale characteristics of the linear relationships between the IO SST and Niño-3.4 index, which are manifested as a positive IOD structure (Fig. S1). These results suggest that the models are capable to capture the statistical connection between the ENSO and IOD.

During the mid-Holocene, the attenuation of the ENSO behavior is consistently indicated by the numerical modelling (Tian et al. 2017; Chen et al. 2019) and proxy-based reconstruction (Tudhope et al. 2001; Thompson et al. 2017), as well as in the present simulations as represented by the reduced standard deviation of the Niño-3.4 index (Fig. 5b). Whether the suppressed ENSO amplitude plays a role in the damping of IOD remains unresolved. We attempt to address this question using a composite analysis. The El Niño/La Niña events are selected when the ASON-mean Niño-3.4 index is greater/less than 0.8/−0.8 standard deviation.

Figure 13 shows the mid-Holocene minus preindustrial changes in composite SST anomalies related to all IOD events ($\Delta SST'_{IOD}$) and to the IOD events that occur independently of ENSO ($\Delta SST'_{IOD\&noENSO}$), as well as their differences. The $\Delta SST'_{IOD}$ contains the effects of the alteration in both the local mean states and remote ENSO activities, while the $\Delta SST'_{IOD\&noENSO}$ removes the impacts from the ENSO change. As such, the difference between $\Delta SST'_{IOD}$ and $\Delta SST'_{IOD\&noENSO}$ manifests the possible impacts of the ENSO diminishment. As shown in Figs. 13a and b, the difference in the multimodel mean is not significant over core IOD regions. Such a result also holds for individual models as indicated by a similar analysis applied to the DMI (Fig. 13c). Accordingly, the suppression of IOD activities during the mid-Holocene is unlikely caused by the ENSO diminishment in the tropical Pacific.

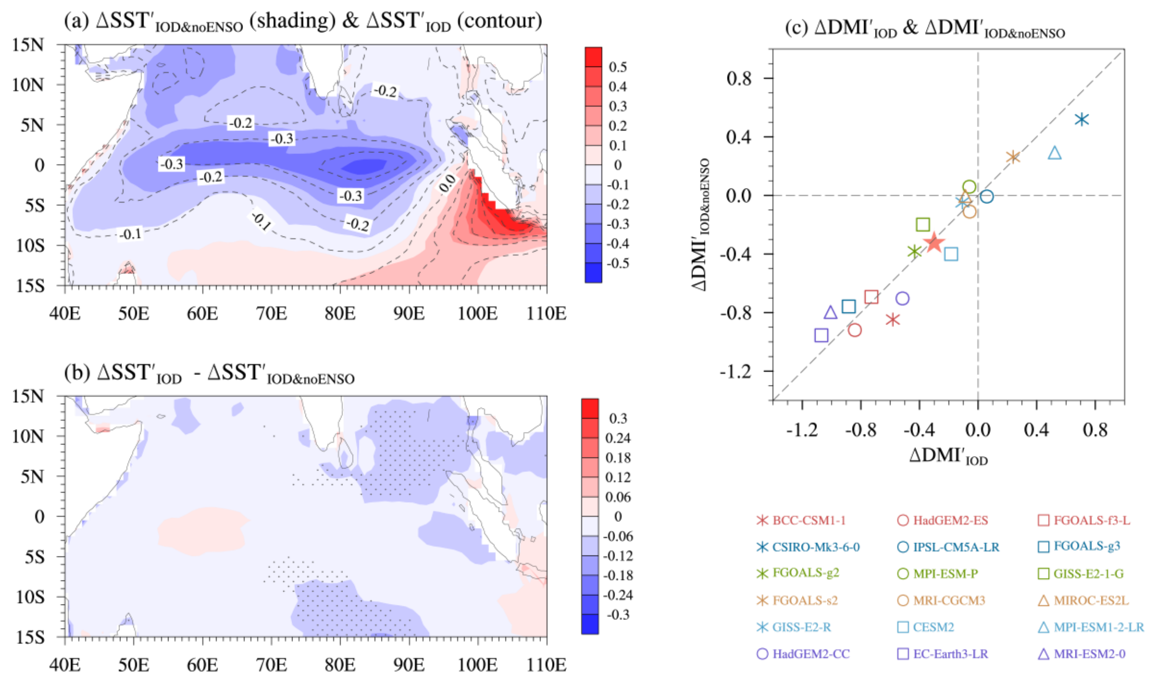

Fig. 13. (a) Multi-model mean changes in composite SST anomalies from the preindustrial period to the mid-Holocene for all IOD events ($\Delta SST'_{IOD}$; contour; same plot as in Fig. 6b) and for IOD events that occur independently of ENSO ($\Delta SST'_{IOD\&noENSO}$; shading) and (b) their differences. (c) Scatter plot of mid-Holocene minus preindustrial period change in DMI anomalies of all IOD events and IOD events that occur

independently of ENSO ($\Delta\mathrm{DMI}'_{\mathrm{IOD}}$ and $\Delta\mathrm{DMI}'_{\mathrm{IOD\&noENSO}}$) in each model. Stippling in (b) indicates regions where the difference is statistically significant at the 95% confidence level. The red star in (c) denotes the multimodel mean of the 18 PMIP3/4 models.

Such a weak relationship between the changes in the two oscillations possibly comes from a weakened connection between the two oscillations themselves. According to the multimodel mean, the correlation coefficient of DMI versus Niño-3.4 index is reduced by 0.07 (from 0.44 to 0.37), statistically significant at the 95% confidence level, meaning that the variance of the DMI explained by the Niño-3.4 index variability is remarkably decreased by 5.7% (from 19.4% to 13.7%). There is also a significantly decreased frequency in the cooccurrence of IOD and ENSO events (Fig. 14), confirming that the IOD is less linked to the ENSO during the mid-Holocene than during the preindustrial period. By contrast, the change in regression coefficient between the two indices is insignificant, indicating that the sensitivity of IOD SST to the ENSO variability seldom alters. Taken together, the impact of the diminished correlation between the IOD and ENSO offsets that of the suppressed ENSO variability, explaining why the ENSO suppression is not forcing on the weakening of the IOD. The aforementioned analysis confirms that the IOD variation during the mid-Holocene arises from the changes in the local mean state and consequently ocean–atmosphere interactions.

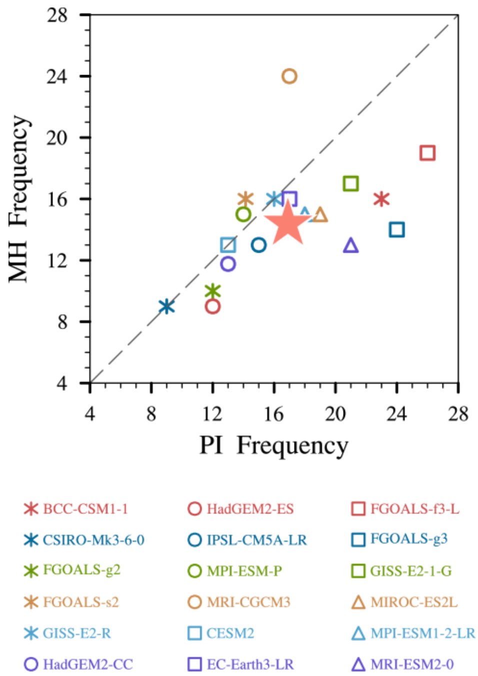

Fig. 14. The co-occurring frequency of IOD and ENSO (number per 100 years) during the preindustrial period (x axis) and mid-Holocene (y axis). The red star denotes the multimodel mean of the 18 PMIP3/4 models.

5. Summary and discussion

The difference in IOD behaviors between the mid-Holocene and preindustrial period is investigated based on numerical experiments undertaken with 18 models from the PMIP3 and PMIP4 frameworks. According to the multimodel mean, the IOD amplitude at the mid-Holocene is 14% below that during the preindustrial period, manifested by the reduced standard deviation of the DMI. The further composite analysis indicates that the weakening of IOD is dominated by the suppressed variability over the western pole, as the IOD-induced SST warming over the WEIO declines by 40% in the multimodel mean with a high agreement across models. The IOD-related cooling in the SEIO alters insignificantly with substantial discrepancies across models, contributing little to the reduction of the DMI standard deviation. Nevertheless, significant negative/positive changes in the IOD-related cooling can be found over CEIO/southern SEIO, indicating a northwestward shift of IOD-related eastern cooling.

The MLHB diagnosis indicates that the aforementioned changes in the IOD-related perturbations mainly arise from the altered climate basic states, which modulate the regional ocean–atmosphere coupled processes over the IO. As responses to increased incoming insolation during IOD growing and peak seasons, there are amplified land–ocean thermal contrasts in both hemispheres, which enhance subtropical anticyclones in the Pacific oceans and subsequently induce strengthened equatorial easterlies across the Indo–Pacific. Such intensified easterlies facilitate a positive IOD-like pattern of the mean-state change, with intensified westward currents across the equatorial IO, as well as enhanced northwestward flows over the SEIO. The intensified westward currents accelerate the anomalous westward advection of the IOD-induced cooling from the eastern pole, predominantly leading to the negative changes of IOD-related SST perturbations over the WEIO and CEIO. The enhanced northwestward flows off the Sumatra–Java coast facilitate the northward advection of IOD-induced thermal anomalies, responsible for the weakened oceanic responses to the IOD over the southern SEIO. In addition, the alterations in mean-state zonal and meridional temperature gradients modulate the thermal advection by anomalous flows, acting as additional mechanisms behind the change in IOD behaviors.

Because the mid-Holocene is a well-known period with subdued ENSO variability compared to the present day, whether the suppressed variability over the tropical Pacific plays a role in the change of IOD is a valuable issue to be addressed (Brown et al. 2009; Cai et al. 2013). The present study suggests that the IOD attenuation is probably not related to the ENSO suppression during the mid-Holocene. This is possibly because the connection between the two oscillations themselves is diminished, as demonstrated by a reduced cooccurrence frequency and a decreased linear relationship. Such a diminished connection means that the IOD variance during the mid-Holocene is less related to ENSO variability compared to the preindustrial period. Taken together, the change in IOD variability is barely explained by the change in ENSO but the change in the mean state of tropical IO and the consequent local air–sea coupling.

The previous simulation using the FOAM also suggests a reduced standard deviation of DMI at the mid-Holocene (Brown et al. 2009), in agreement with the present work. Conversely, based on the MIROC5.2, Iwakiri and Watanabe (2019) have suggested that the IOD is intensified at the mid-Holocene, manifested by enhanced SST variability over the EEIO and westward extension of the negative SST anomalies associated with the positive IOD. They attributed the IOD change to the enhanced zonal advective cooling due to changes in the mean currents, which benefit the growth of cooling perturbation in the EEIO. In comparison with Iwakiri and Watanabe (2019), our simulation agrees that the primary mechanism arises from the change in the zonal advection term, which leads to the westward-expanded eastern cooling pole; however, the altered zonal advection term exerts small impacts over the whole SEIO region, insufficient to drive an enhancement of SST variability as claimed in Iwakiri and Watanabe (2019). This discrepancy might come from the difference in the experimental design of orbital parameters, which are fixed at 6 ka in the PMIP experiments but at 8 ka in Iwakiri and Watanabe (2019). Another possible explanation of such a discrepancy is the different model biases (Cai and Cowan 2013) that might lead to intermodel differences in the simulated IOD change.

Finally, the confidence in projecting IOD behaviors requires the validation of climate models, which is limited by the lack of long-term instrumental observations at this state. Here, the mid-Holocene that involves abundant reconstructions and simulations provides an opportunity to counter such a limitation. The simulated mean-state change in the mid-Holocene, which is characterized by a positive IOD-like mode in precipitation and SST, can be evidenced by diverse types of paleo-data. Concerning the IOD-induced SST perturbation, there is also model–data agreement at the data location off the Sumatra coast (Abram et al. 2007). Of note is that solely one proxy site from the eastern IO sector is insufficient to depict the spatial structure change of the IOD SST variability, especially when we show that the change is not spatially uniform. Future supplementary of proxy records in other sectors is expected to verify the IOD variation simulated in our study.

Acknowledgments

We sincerely acknowledge the NOAA PSL for providing the NOAA Extended Reconstructed SST V5 data, as well as the climate modeling groups (listed in Table 1) for producing and sharing their model outputs. This work is supported by the National Natural Science Foundation of China (42088101 and 42105045). The authors declare that they have no conflict of interest.

Data Availability Statement.

The PMIP3 and PMIP4 data are available at https://esgf-node.llnl.gov/projects/cmip5/ and https://esgf-node.llnl.gov/projects/cmip6/, respectively. The ERSST version 5 data are obtained from https://psl.noaa.gov/data/gridded/data.noaa.ersst.v5.html. The proxy data are from peer-reviewed journals listed in Table 3 and the GLSDB (Kohfeld and Harrison 2000).

REFERENCES

Abram, N. J., M. K. Gagan, M. T. McCulloch, J. Chappell, and W. S. Hantoro, 2003: Coral reef death during the 1997 Indian Ocean Dipole linked to Indonesian wildfires. *Science*, **301,** 952–955, https://doi.org/10.1126/science.1083841.

Abram, N. J., M. K. Gagan, J. E. Cole, W. S. Hantoro, and M. Mudelsee, 2008: Recent intensification of tropical climate variability in the Indian Ocean. *Nat. Geosci.*, **1,** 849–853, https://doi.org/10.1038/ngeo357.

Abram, N. J., M. K. Gagan, Z. Liu, W. S. Hantoro, M. T. McCulloch, and B. W. Suwargadi, 2007: Seasonal characteristics of the Indian Ocean Dipole during the Holocene epoch. *Nature*, **445,** 299–302, https://doi.org/10.1038/nature05477.

Abram, N. J., J. A. Hargreaves, N. M. Wright, K. Thirumalai, C. C. Ummenhofer, and M. H. England, 2020a: Palaeoclimate perspectives on the Indian Ocean Dipole. *Quat. Sci. Rev.*, **237,** 106302, https://doi.org/10.1016/j.quascirev.2020.106302.

Abram, N. J., and Coauthors, 2020b: Coupling of Indo-Pacific climate variability over the last millennium. *Nature*, **579,** 385–392, https://doi.org/10.1038/s41586-020-2084-4.

An, S.-I., 2004: A dynamic link between the basin-scale and zonal modes in the Tropical Indian Ocean. *Theor. Appl. Climatol.*, **78,** 203–215, https://doi.org/10.1007/s00704-003-0027-2.

An, S.-I., H.-J. Park, S.-K. Kim, J. Shin, S.-W. Yeh, and J.-S. Kug, 2022: Intensity changes of Indian Ocean Dipole mode in a carbon dioxide removal scenario. *npj Clim. Atmos. Sci.*, **5,** 20, https://doi.org/10.1038/s41612-022-00246-6.

Anand, P., D. Kroon, A. D. Singh, R. S. Ganeshram, G. Ganssen, and H. Elderfield, 2008: Coupled sea surface temperature–seawater $\delta^{18}O$ reconstructions in the Arabian Sea at the millennial scale for the last 35 ka. *Paleoceanography*, **23,** PA4207, https://doi.org/10.1029/2007PA001564.

Bard, E., F. Rostek, and C. Sonzogni, 1997: Interhemispheric synchrony of the last deglaciation inferred from alkenone palaeothermometry. *Nature*, **385,** 707–710, https://doi.org/10.1038/385707a0.

Barker, P. A., and Coauthors, 2001: A 14,000-year oxygen isotope record from diatom silica in two alpine lakes on Mt. Kenya. *Science*, **292,** 2307–2310, https://doi.org/10.1126/science.1059612.

Behera, S. K., J. J. Luo, S. Masson, S. A. Rao, H. Sakuma, and T. Yamagata, 2006: A CGCM study on the interaction between IOD and ENSO. *J. Climate*, **19**, 1688–1705, https://doi.org/10.1175/jcli3797.1.

Berger, A. L., 1978: Long-term variations of daily insolation and quaternary climatic changes. *J. Atmos. Sci.*, **35,** 2362–2367, https://doi.org/10.1175/1520-0469(1978)035<2362:ltvodi>2.0.co;2.

Bjerknes, J., 1969: Atmospheric teleconnections from the equatorial Pacific. *Mon. Wea. Rev.*, **97,** 163–172, https://doi.org/10.1175/1520-0493(1969)097<0163:atftep>2.3.co;2.

Brierley, C. M., and Coauthors, 2020: Large-scale features and evaluation of the PMIP4-CMIP6 midHolocene simulations. *Climate Past*, **16,** 1847–1872, https://doi.org/10.5194/cp-16-1847-2020.

Brown, J., A. H. Lynch, and A. G. Marshall, 2009: Variability of the Indian Ocean Dipole in coupled model paleoclimate simulations. *J. Geophys. Res.*, **114,** D11105, https://doi.org/10.1029/2008JD010346.

Cai, W., and T. Cowan, 2013: Why is the amplitude of the Indian Ocean Dipole overly large in CMIP3 and CMIP5 climate models? *Geophys. Res. Lett.*, **40,** 1200–1205, https://doi.org/10.1002/grl.50208.

Cai, W., and Coauthors, 2013: Projected response of the Indian Ocean Dipole to greenhouse warming. *Nat. Geosci.*, **6,** 999–1007, https://doi.org/10.1038/ngeo2009.

Cai, W., and Coauthors, 2014: Increased frequency of extreme Indian Ocean Dipole events due to greenhouse warming. *Nature*, **510,** 254–258, https://doi.org/10.1038/nature13327.

Cai, W., and Coauthors, 2019: Pantropical climate interactions. *Science*, **363,** eaav4236, https://doi.org/10.1126/science.aav4236.

Chen, L., W. Zheng, and P. Braconnot, 2019: Towards understanding the suppressed ENSO activity during mid-Holocene in PMIP2 and PMIP3 simulations. *Climate Dyn*, **53,** 1095–1110, https://doi.org/10.1007/s00382-019-04637-z.

Chu, J.-E., K.-J. Ha, J.-Y. Lee, B. Wang, B.-H. Kim, and C. E. Chung, 2014: Future change of the Indian Ocean basin-wide and dipole modes in the CMIP5. *Climate Dyn*, **43,** 535–551, https://doi.org/10.1007/s00382-013-2002-7.

Cui, K., Y. Wang, X. Liu, J. Shen, and Y. Wang, 2022: Holocene variation in the Indian Summer Monsoon modulated by the tropical Indian Ocean sea-surface temperature mode. *Catena*, **215,** 106302, https://doi.org/10.1016/j.catena.2022.106302.

Fischer, A. S., P. Terray, E. Guilyardi, S. Gualdi, and P. Delecluse, 2005: Two independent triggers for the Indian Ocean Dipole/Zonal Mode in a coupled GCM. *J. Climate*, **18,** 3428–3449, https://doi.org/10.1175/jcli3478.1.

Foerster, V., and Coauthors, 2012: Climatic change recorded in the sediments of the Chew Bahir basin, southern Ethiopia, during the last 45,000 years. *Quat. Int.*, **274,** 25–37, https://doi.org/10.1016/j.quaint.2012.06.028.

Garcin, Y., D. Melnick, M. R. Strecker, D. Olago, and J.-J. Tiercelin, 2012: East African mid-Holocene wet–dry transition recorded in palaeo-shorelines of Lake Turkana, northern Kenya Rift. *Earth Planet. Sci. Lett.*, **331–332,** 322–334, https://doi.org/10.1016/j.epsl.2012.03.016.

Garcin, Y., A. Junginger, D. Melnick, D. O. Olago, M. R. Strecker, and M. H. Trauth, 2009: Late Pleistocene–Holocene rise and collapse of Lake Suguta, northern Kenya Rift. *Quat. Sci. Rev.*, **28,** 911–925, https://doi.org/10.1016/j.quascirev.2008.12.006.

Gasse, F., 2000: Hydrological changes in the African tropics since the Last Glacial Maximum. *Quat. Sci. Rev.*, **19,** 189–211, https://doi.org/10.1016/S0277-3791(99)00061-X.

Griffiths, M. L., and Coauthors, 2010: Evidence for Holocene changes in Australian–Indonesian monsoon rainfall from stalagmite trace element and stable isotope ratios. *Earth Planet. Sci. Lett.*, **292,** 27–38, https://doi.org/10.1016/j.epsl.2010.01.002.

Hashizume, M., L. F. Chaves, and N. Minakawa, 2012: Indian Ocean Dipole drives malaria resurgence in East African highlands. *Sci. Rep.*, **2,** 269, https://doi.org/10.1038/srep00269.

He, C., and W. Zhou, 2020: Different enhancement of the East Asian Summer Monsoon under global warming and interglacial epochs simulated by CMIP6 models: Role of the subtropical high. *J. Climate*, **33,** 9721–9733, https://doi.org/10.1175/jcli-d-20-0304.1.

Huang, B., and Coauthors, 2017: Extended reconstructed sea surface temperature, version 5 (ERSSTv5): Upgrades, validations, and intercomparisons. *J. Climate*, **30,** 8179–8205, https://doi.org/10.1175/jcli-d-16-0836.1.

Huguet, C., J.-H. Kim, J. S. Sinninghe Damsté, and S. Schouten, 2006: Reconstruction of sea surface temperature variations in the Arabian Sea over the last 23 kyr using organic proxies (TEX86 and U37K’). *Paleoceanography*, **21,** PA3003, https://doi.org/10.1029/2005PA001215.

Ihara, C., Y. Kushnir, and M. A. Cane, 2008: Warming Trend of the Indian Ocean SST and Indian Ocean Dipole from 1880 to 2004. *J. Climate*, **21,** 2035–2046, https://doi.org/10.1175/2007jcli1945.1.

Iwakiri, T., and M. Watanabe, 2019: Strengthening of the Indian Ocean Dipole with increasing seasonal cycle in the mid-Holocene. *Geophys. Res. Lett.*, **46,** 8320–8328, https://doi.org/10.1029/2019GL083088.

King, A. D., A. J. Pitman, B. J. Henley, A. M. Ukkola, and J. R. Brown, 2020: The role of climate variability in Australian drought. *Nat. Climate Change*, **10,** 177–179, https://doi.org/10.1038/s41558-020-0718-z.

Kohfeld, K. E., and S. P. Harrison, 2000: How well can we simulate past climates? Evaluating the models using global palaeoenvironmental datasets. *Quat. Sci. Rev.*, **19,** 321–346, https://doi.org/10.1016/S0277-3791(99)00068-2.

Kuhnert, H., H. Kuhlmann, M. Mohtadi, H. Meggers, K.-H. Baumann, and J. Pätzold, 2014: Holocene tropical western Indian Ocean sea surface temperatures in covariation with climatic changes in the Indonesian region. *Paleoceanography*, **29,** 423–437, https://doi.org/10.1002/2013PA002555.

Lau, N.-C., and M. J. Nath, 2004: Coupled GCM simulation of atmosphere–ocean variability associated with zonally asymmetric SST changes in the tropical Indian Ocean. *J. Climate*, **17,** 245–265, https://doi.org/10.1175/1520-0442(2004)017<0245:Cgsoav>2.0.Co;2.

Li, G., S. P. Xie, and Y. Du, 2016a: A robust but spurious pattern of climate change in model projections over the tropical Indian Ocean. *J. Climate*, **29,** 5589–5608, https://doi.org/10.1175/jcli-d-15-0565.1.

Li, T., Y. Zhang, E. Lu, and D. Wang, 2002: Relative role of dynamic and thermodynamic processes in the development of the Indian Ocean dipole: An OGCM diagnosis. *Geophys. Res. Lett.*, **29,** 25-21–25-24, https://doi.org/10.1029/2002GL015789.

Li, T., B. Wang, C.-P. Chang, and Y. Zhang, 2003: A theory for the Indian Ocean Dipole–Zonal Mode. *J. Atmos. Sci.*, **60,** 2119–2135, https://doi.org/10.1175/1520-0469(2003)060<2119:Atftio>2.0.Co;2.

Li, Z., and Coauthors, 2016b: Late Quaternary fingerprints of precession and sea level variation over the past 35 kyr as revealed by sea surface temperature and upwelling records from the Indian Ocean near southernmost Sumatra. *Quat. Int.*, **425,** 282–291, https://doi.org/10.1016/j.quaint.2016.07.013.

Liu, L., S.-P. Xie, X.-T. Zheng, T. Li, Y. Du, G. Huang, and W.-D. Yu, 2014: Indian Ocean variability in the CMIP5 multi-model ensemble: The zonal dipole mode. *Climate Dyn*, **43,** 1715–1730, https://doi.org/10.1007/s00382-013-2000-9.

Liu, S., D. Jiang, and X. Lang, 2019: Mid-Holocene drylands: A multi-model analysis using Paleoclimate Modelling Intercomparison Project Phase III (PMIP3) simulations. *Holocene*, **29,** 1425–1438, https://doi.org/10.1177/0959683619854512.

Lohmann, G., M. Pfeiffer, T. Laepple, G. Leduc, and J.-H. Kim, 2013: A model–data comparison of the Holocene global sea surface temperature evolution. *Climate Past*, **9,** 1807–1839, https://doi.org/10.5194/cp-9-1807-2013.

Lu, B., and Coauthors, 2018: An extreme negative Indian Ocean Dipole event in 2016: Dynamics and predictability. *Climate Dyn*, **51,** 89–100, https://doi.org/10.1007/s00382-

017-3908-2.

Lückge, A., M. Mohtadi, C. Rühlemann, G. Scheeder, A. Vink, L. Reinhardt, and M. Wiedicke, 2009: Monsoon versus ocean circulation controls on paleoenvironmental conditions off southern Sumatra during the past 300,000 years. *Paleoceanography*, **24,** PA1208, https://doi.org/10.1029/2008PA001627.

Luo, J.-J., R. Zhang, S. K. Behera, Y. Masumoto, F.-F. Jin, R. Lukas, and T. Yamagata, 2010: Interaction between El Niño and extreme Indian Ocean Dipole. *J. Climate*, **23**, 726–742, https://doi.org/10.1175/2009jcli3104.1.

Marathe, S., P. Terray, and A. Karumuri, 2021: Tropical Indian Ocean and ENSO relationships in a changed climate. *Climate Dyn*, **56,** 3255–3276, https://doi.org/10.1007/s00382-021-05641-y.

Marchant, R., C. Mumbi, S. Behera, and T. Yamagata, 2007: The Indian Ocean dipole – the unsung driver of climatic variability in East Africa. *Afr. J. Ecol.*, **45,** 4–16, https://doi.org/10.1111/j.1365-2028.2006.00707.x.

Mohtadi, M., S. Steinke, A. Lückge, J. Groeneveld, and E. C. Hathorne, 2010: Glacial to Holocene surface hydrography of the tropical eastern Indian Ocean. *Earth Planet. Sci. Lett.*, **292,** 89–97, https://doi.org/10.1016/j.epsl.2010.01.024.

Mohtadi, M., and Coauthors, 2014: North Atlantic forcing of tropical Indian Ocean climate. *Nature*, **509,** 76–80, https://doi.org/10.1038/nature13196.

Nakamura, N., H. Kayanne, H. Iijima, T. R. McClanahan, S. K. Behera, and T. Yamagata, 2009: Mode shift in the Indian Ocean climate under global warming stress. *Geophys. Res. Lett.*, **36,** L23708, https://doi.org/10.1029/2009GL040590.

Niedermeyer, E. M., A. L. Sessions, S. J. Feakins, and M. Mohtadi, 2014: Hydroclimate of the western Indo-Pacific Warm Pool during the past 24,000 years. *Proc. Natl. Acad. Sci. USA*, **111,** 9402–9406, https://doi.org/10.1073/pnas.1323585111.

Otto-Bliesner, B. L., and Coauthors, 2017: The PMIP4 contribution to CMIP6 – part 2: two interglacials, scientific objective and experimental design for Holocene and last interglacial simulations. *Geosci. Model Dev.*, **10,** 3979–4003, https://doi.org/10.5194/gmd-10-3979-2017.

Rao, S. A., S. Masson, J.-J. Luo, S. K. Behera, and T. Yamagata, 2007: Termination of Indian Ocean Dipole events in a coupled general circulation model. *J. Climate*, **20**, 3018–3035, https://doi.org/10.1175/jcli4164.1.

Rasmusson, E. M., and T. H. Carpenter, 1982: Variations in tropical sea surface temperature and surface wind fields associated with the Southern Oscillation/El Niño. *Mon. Wea. Rev.*,

110, 354–384, https://doi.org/10.1175/1520-0493(1982)110<0354:Vitsst>2.0.Co;2.

Raza, T., S. M. Ahmad, S. Steinke, W. Raza, M. A. Lone, S. K. Beja, and G. Suseela, 2017: Glacial to Holocene changes in sea surface temperature and seawater $\delta^{18}O$ in the northern Indian Ocean. *Palaeogeogr., Palaeoclimatol., Palaeoecol.*, **485,** 697–705, https://doi.org/10.1016/j.palaeo.2017.07.026.

Romahn, S., A. Mackensen, J. Groeneveld, and J. Pätzold, 2014: Deglacial intermediate water reorganization: New evidence from the Indian Ocean. *Climate Past*, **10,** 293–303, https://doi.org/10.5194/cp-10-293-2014.

Rostek, F., G. Ruhlandt, F. C. Bassinot, P. J. Muller, L. D. Labeyrie, Y. Lancelot, and E. Bard, 1993: Reconstructing sea surface temperature and salinity using $\delta^{18}O$ and alkenone records. *Nature*, **364,** 319–321, https://doi.org/10.1038/364319a0.

Saji, N. H., 2018: The Indian Ocean Dipole. Oxford Research Encyclopedia of Climate Science. https://doi.org/10.1093/acrefore/9780190228620.013.619.

Saji, N. H., B. N. Goswami, P. N. Vinayachandran, and T. Yamagata, 1999: A dipole mode in the tropical Indian Ocean. *Nature*, **401,** 360–363, https://doi.org/10.1038/43854.

Schott, F. A., S.-P. Xie, and J. P. McCreary Jr., 2009: Indian Ocean circulation and climate variability. *Rev. Geophys.*, **47,** RG1002, https://doi.org/10.1029/2007RG000245.

Stuecker, M. F., and Coauthors, 2017: Revisiting ENSO/Indian Ocean Dipole phase relationships. *Geophys. Res. Lett.*, **44,** 2481–2492, https://doi.org/10.1002/2016GL072308.

Thompson, D. M., and Coauthors, 2017: Tropical Pacific climate variability over the last 6000 years as recorded in Bainbridge Crater Lake, Galápagos. *Paleoceanography*, **32,** 903–922, https://doi.org/10.1002/2017PA003089.

Thompson, L. G., and Coauthors, 2002: Kilimanjaro ice core records: Evidence of Holocene climate change in tropical Africa. *Science*, **298,** 589–593, https://doi.org/10.1126/science.1073198.

Tian, Z., T. Li, and D. Jiang, 2018: Strengthening and westward shift of the tropical Pacific Walker Circulation during the mid-Holocene: PMIP simulation results. *J. Climate*, **31,** 2283–2298, https://doi.org/10.1175/jcli-d-16-0744.1.

Tian, Z., T. Li, D. Jiang, and L. Chen, 2017: Causes of ENSO weakening during the mid-Holocene. *J. Climate*, **30,** 7049–7070, https://doi.org/10.1175/jcli-d-16-0899.1.

Tierney, J. E., S. C. Lewis, B. I. Cook, A. N. LeGrande, and G. A. Schmidt, 2011: Model, proxy and isotopic perspectives on the East African Humid Period. *Earth Planet. Sci. Lett.*, **307,** 103–112, https://doi.org/10.1016/j.epsl.2011.04.038.

Tudhope, A. W., and Coauthors, 2001: Variability in the El Niño–Southern Oscillation through a glacial–interglacial cycle. *Science*, **291,** 1511–1517, https://doi.org/10.1126/science.1057969.

Ummenhofer, C. C., and Coauthors, 2009: What causes southeast Australia's worst droughts? *Geophys. Res. Lett.*, **36,** L04706, https://doi.org/10.1029/2008GL036801.

Webster, P. J., A. M. Moore, J. P. Loschnigg, and R. R. Leben, 1999: Coupled ocean–atmosphere dynamics in the Indian Ocean during 1997–98. *Nature*, **401,** 356–360, https://doi.org/10.1038/43848.

Weldeab, S., C. Rühlemann, Q. Ding, V. Khon, B. Schneider, and W. R. Gray, 2022: Impact of Indian Ocean surface temperature gradient reversals on the Indian Summer Monsoon. *Earth Planet. Sci. Lett.*, **578,** 117327, https://doi.org/10.1016/j.epsl.2021.117327.

Xie, S. P., and S. G. H. Philander, 1994: A coupled ocean–atmosphere model of relevance to the ITCZ in the eastern Pacific. *Tellus A*, **46,** 340–350, https://doi.org/10.1034/j.1600-0870.1994.t01-1-00001.x.

Yamagata, T., S. K. Behera, J.-J. Luo, S. Masson, M. R. Jury, and S. A. Rao, 2004: Coupled ocean–atmosphere variability in the tropical Indian Ocean. *Earth's Climate: The Ocean–Atmosphere Interaction*, C. Wang, S. P. Xie, and J. A. Carton, Eds., American Geophysical Union Geophysical Monograph Series, 189–211, https://doi.org/10.1029/147GM12.

Yang, W., R. Seager, M. A. Cane, and B. Lyon, 2015: The annual cycle of East African precipitation. *J. Climate*, **28,** 2385–2404, https://doi.org/10.1175/jcli-d-14-00484.1.

Yuan, C., W. Li, Z. Guan, and T. Yamagata, 2019: Impacts of April snow cover extent over Tibetan Plateau and the central Eurasia on Indian Ocean Dipole. *Int. J. Climatol.*, **39**, 1756–1767, https://doi.org/10.1002/joc.5888.

Zhang, W., Y. Wang, F.-F. Jin, M. F. Stuecker, and A. G. Turner, 2015: Impact of different El Niño types on the El Niño/IOD relationship. *Geophys. Res. Lett.*, **42,** 8570–8576, https://doi.org/10.1002/2015GL065703.

Zheng, X.-T., S.-P. Xie, Y. Du, L. Liu, G. Huang, and Q. Liu, 2013: Indian Ocean Dipole response to global warming in the CMIP5 multimodel ensemble. *J. Climate*, **26,** 6067–6080, https://doi.org/10.1175/jcli-d-12-00638.1.

Zinke, J., and Coauthors, 2014: Seychelles coral record of changes in sea surface temperature bimodality in the western Indian Ocean from the mid-Holocene to the present. *Climate Dyn*, **43,** 689–708, https://doi.org/10.1007/s00382-014-2082-z.

SUPPLEMENTAL MATERIAL

Weakening of the Indian Ocean Dipole in the mid-Holocene due to the mean oceanic climatology change

Shanshan Liu[a], Chaoxia Yuan[a], Jing-jia Luo[a], Xiaofan Ma[a], Xuecheng Zhou[b], Toshio Yamagata[a, c]

[a] *Collaborative Innovation Center on Forecast and Evaluation of Meteorological Disasters (CIC-FEMD)/Institute for Climate and Application Research (ICAR), Nanjing University of Information Science and Technology, Nanjing, China*

[b] *Meteorological Service Center of Jiangsu Province, Nanjing, China*

[c] *Application Laboratory, Research Institute for Value-Added-Information Generation, Japan Agency for Marine–Earth Science and Technology, Yokohama, Japan*

Corresponding author: Shanshan Liu (E-mail: liushanshan@nuist.edu.cn)

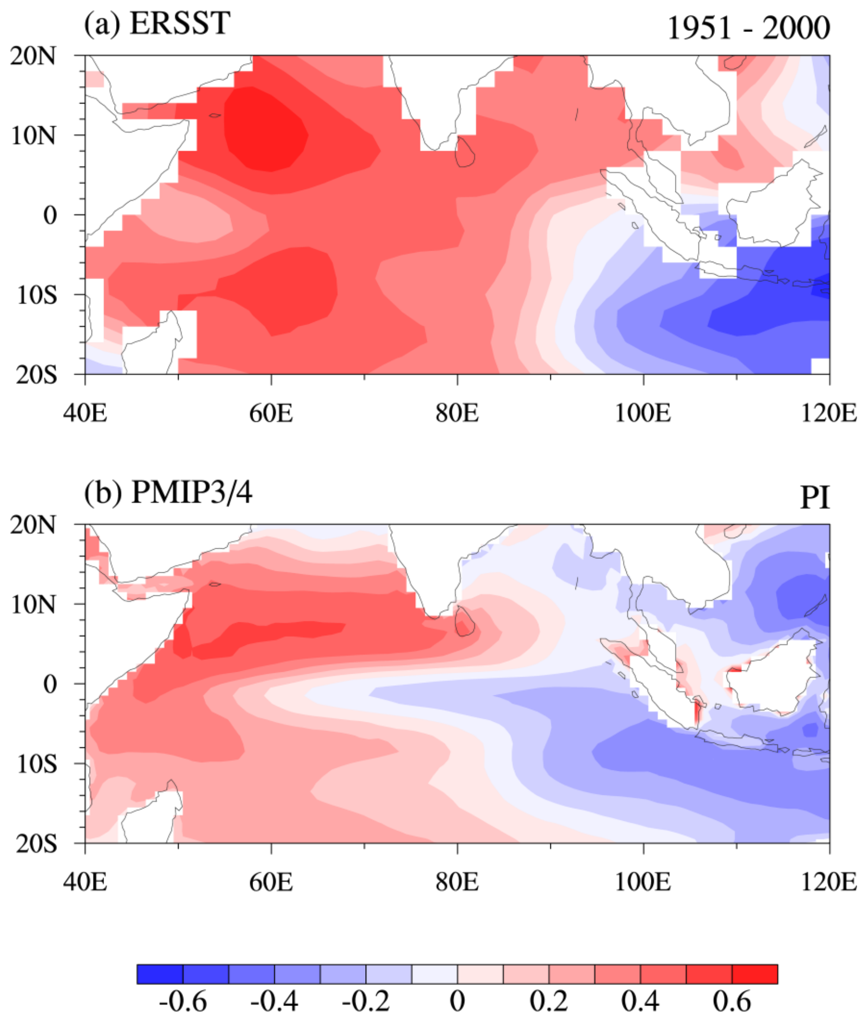

Fig. S1. Correlation coefficients between the Niño-3.4 SST index and SST in the IO based on (a) ERSST data in the period 1951–2000 and (b) the multimodel mean during the preindustrial period.

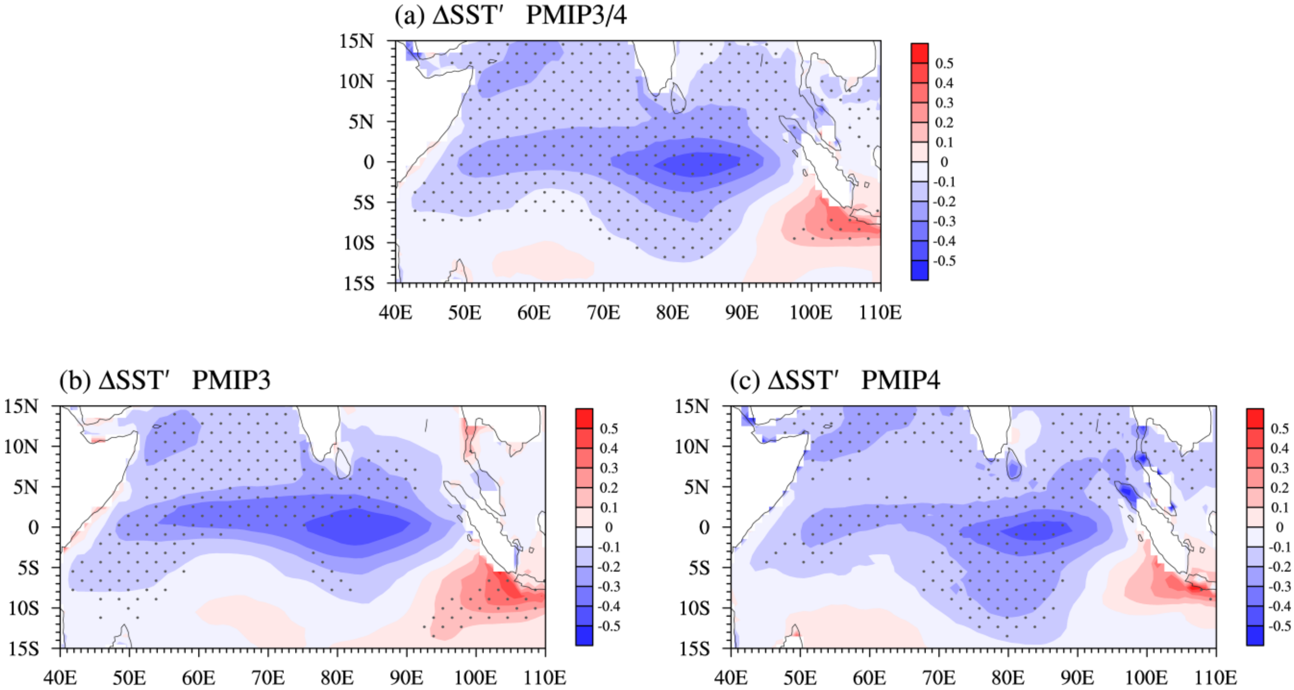

Fig. S2. The mid-Holocene minus preindustrial period difference in IOD composite SST anomalies (ΔSST′) during ASON based on total 30 models within the PMIP3 and PMIP4 frameworks. (a) The 30-model mean of the combined PMIP3 and PMIP4 models, (b) the 14-model mean of PMIP3 models, and (c) the 16-model mean of PMIP4 models. The stippling indicates regions where the change is statistically significant at the 95% confidence level. Here, the PMIP3 models include CCSM4, CNRM-CM5, CSIRO-Mk3L-1-2, MIROC-ESM, and other 10 models listed in Table 1. PMIP4 models involve ACCESS-ESM1-5, AWI-ESM-1-1-LR, HadGEM3-GC31-LL, INM-CM4-8, IPSL-CM6A-LR, NESM3, NorESM1-F, NorESM2-LM, and other 8 models listed in Table 1.

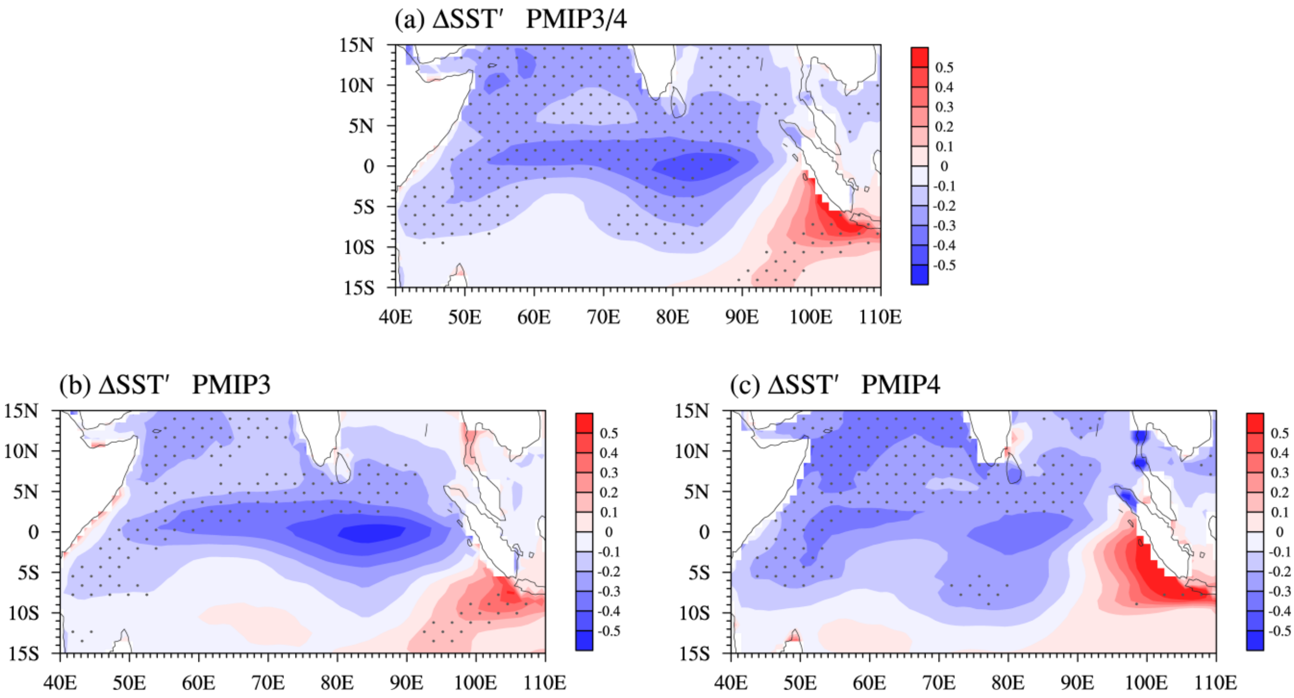

Fig. S3. Same as Fig. S2, but based on the 18-model subset used in our study. (a) The 18-model mean of the combined PMIP3 and PMIP3 models, (b) 10-model mean of PMIP3 models, and (c) 8-model mean of PMIP4 models.